Post-collisional magmatism associated with the final closure of the Rushan-Pshart Meso-Tethys Ocean in Pamir, Tajikistan: Inference from Cretaceous igneous rocks of the Pshart accretionary complex

Dzhovid Yogibekov[1,2,3], Miao Sang[1]*, Wenjiao Xiao[1,2]*, Yunus Mamadjonov[3,4], Chuanming Zhou[5], He Yang[1], Qigui Mao[1], Jovid Aminov[6], Gufron Khalimov[1,3] and Sohibnazar Ashuraliev[1,3]

[1]Xinjiang Key Laboratory of Mineral Resources and Digital Geology, Xinjiang Institute of Geology and Geography, Chinese Academy of Science, Urumqi, China, [2]Collage of Earth and Planetary Sciences, University of Chinese Academy of Sciences, Beijing, China, [3]Institute of Geology, Earthquake Engineering and Seismology, Academy of Sciences of the Republic of Tajikistan, Dushanbe, Tajikistan, [4]Research Center for Ecology and Environment of Central Asia, Chinese Academy of Sciences, Dushanbe, Tajikistan, [5]Research Institute of Petroleum Exploration and Development, China National Petroleum Corporation, Beijing, China, [6]University of Central Asia, Khorog, Tajikistan

The Pamir orogen was formed by the subducted accretion and amalgamation of Cimmerian terranes from the northern margin of Gondwana with the southern margin of Eurasia. The Mesozoic magmatic rocks are widespread in Pamir and record the tectonic evolution in different stages. The Rushan−Pshart suture zone represents an ancient ocean between Central and Southern Pamir. This paper reports the petrography, geochronology, and geochemistry of Cretaceous granites and diabase dikes that intrude into the Pshart complex. The granites were emplaced between 124 and 118 Ma, based on their zircon U-Pb ages. These granites are characterized by high-K calc-alkaline, low magnesian, and high SiO_2, A/CNK, and K_2O+Na_2O values. They also display strong depletion of Ba, Sr, Eu, and Ti and comparatively weak negative Nb anomalies in spidergrams. Thus, we proposed in this study that these are highly fractionated, strongly peraluminous S-type granites. They were generated by the partial melting of the metasedimentary rocks in the plagioclase stability field and underwent subsequent fractional crystallization during their ascent. The diabase dikes contain low SiO_2, and high MgO levels and negative Nb and Ta anomalies, which were interpreted to form in an extensional environment. Late Jurassic−Early Cretaceous closure of the Rushan−Pshart Ocean and subsequent foundering of its oceanic lithosphere caused local extension and upwelling of the asthenospheric mantle. The underplating of mafic magma provided a heat source to melt the metasedimentary-derived granitic that formed in the initial post-collisional

environment. The subsequent local extension caused the emplacement of diabase dikes. Based on our new data and combined with data from previous studies, we concluded that the Rushan−Pshart suture zone is the remnant of the Meso-Tethys Ocean and may represent the western continuation of the Bangong−Nujiang suture of the Tibetan Plateau.

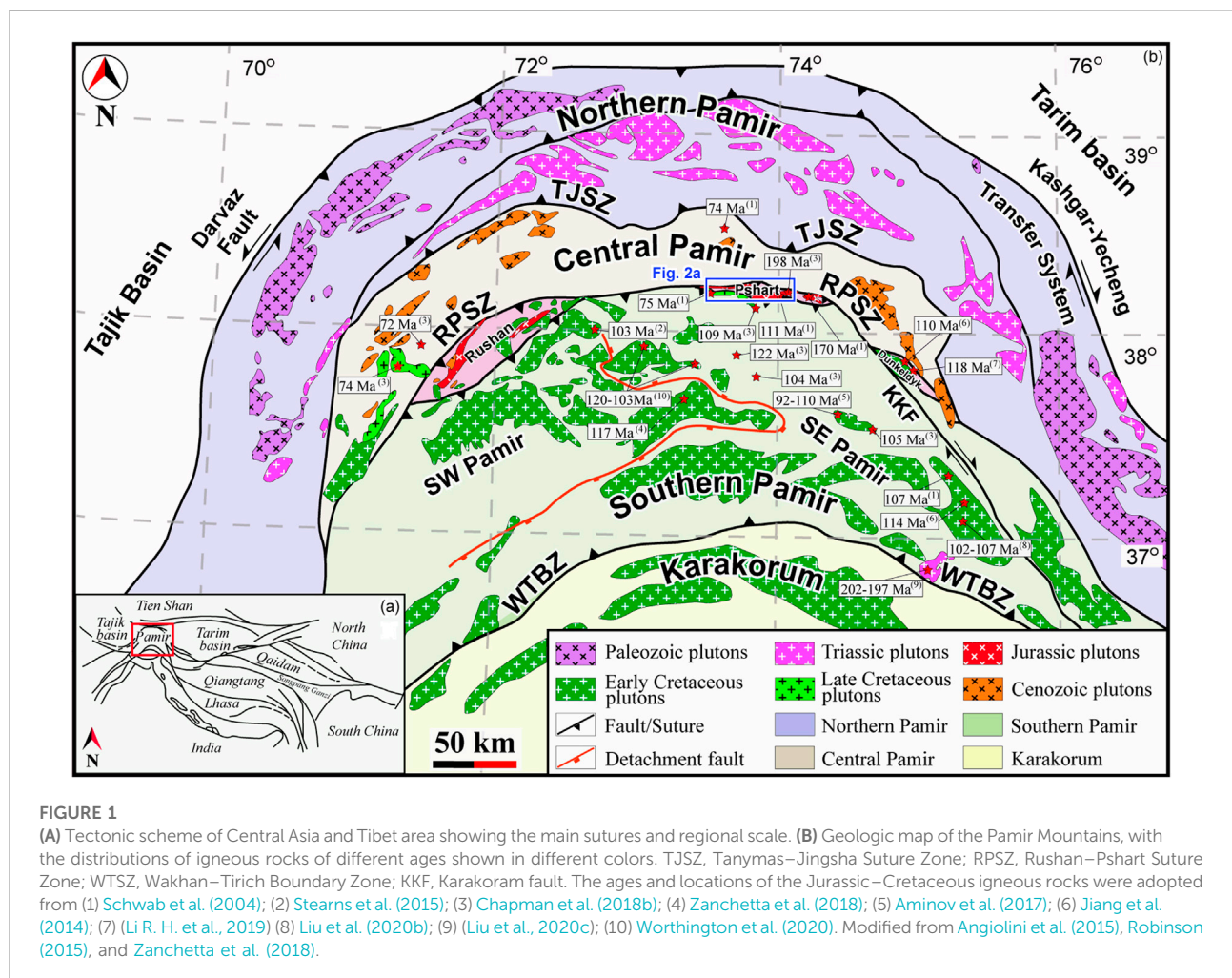# 1 Introduction

The Pamir orogenic belt, located west to the Himalayan−Tibet orogen, was formed by the closure of the Paleo and Meso-Tethyan Oceans and the amalgamation of microcontinents derived from Gondwana supercontinent (Central Pamir, South Pamir, Karakoram terrane, and the Cimmerian blocks) to the southern margin of Eurasia during the early Mesozoic (Burtman and Molnar, 1993; Zanchi et al., 2000, 2009; Burtman, 2010; Zanchi and Gaetani, 2011). The

Rushan−Pshart suture zone (RPSZ) lies in the Pamir orogen; it represents the tectonic boundary separating the Central and Southern Pamir terranes (Figure 1) and preserves the remnants of consumed Rushan−Pshart Ocean (Shvol'man, 1978; Pashkov and Shvol'man, 1979; Burtman and Molnar, 1993; Leven, 1995; Burtman, 2010; Yogibekov et al., 2020).

Two controversial hypotheses/models have been proposed regarding the evolution and closure timing of the Rushan−Pshart Ocean. One group of studies reported a Late Triassic−Early Jurassic closure time for the Rushan−Pshart Ocean (Angiolini

FIGURE 1
(A) Tectonic scheme of Central Asia and Tibet area showing the main sutures and regional scale. **(B)** Geologic map of the Pamir Mountains, with the distributions of igneous rocks of different ages shown in different colors. TJSZ, Tanymas−Jingsha Suture Zone; RPSZ, Rushan−Pshart Suture Zone; WTSZ, Wakhan−Tirich Boundary Zone; KKF, Karakoram fault. The ages and locations of the Jurassic−Cretaceous igneous rocks were adopted from (1) Schwab et al. (2004); (2) Stearns et al. (2015); (3) Chapman et al. (2018b); (4) Zanchetta et al. (2018); (5) Aminov et al. (2017); (6) Jiang et al. (2014); (7) (Li R. H. et al., 2019) (8) Liu et al. (2020b); (9) (Liu et al., 2020c); (10) Worthington et al. (2020). Modified from Angiolini et al. (2015), Robinson (2015), and Zanchetta et al. (2018).
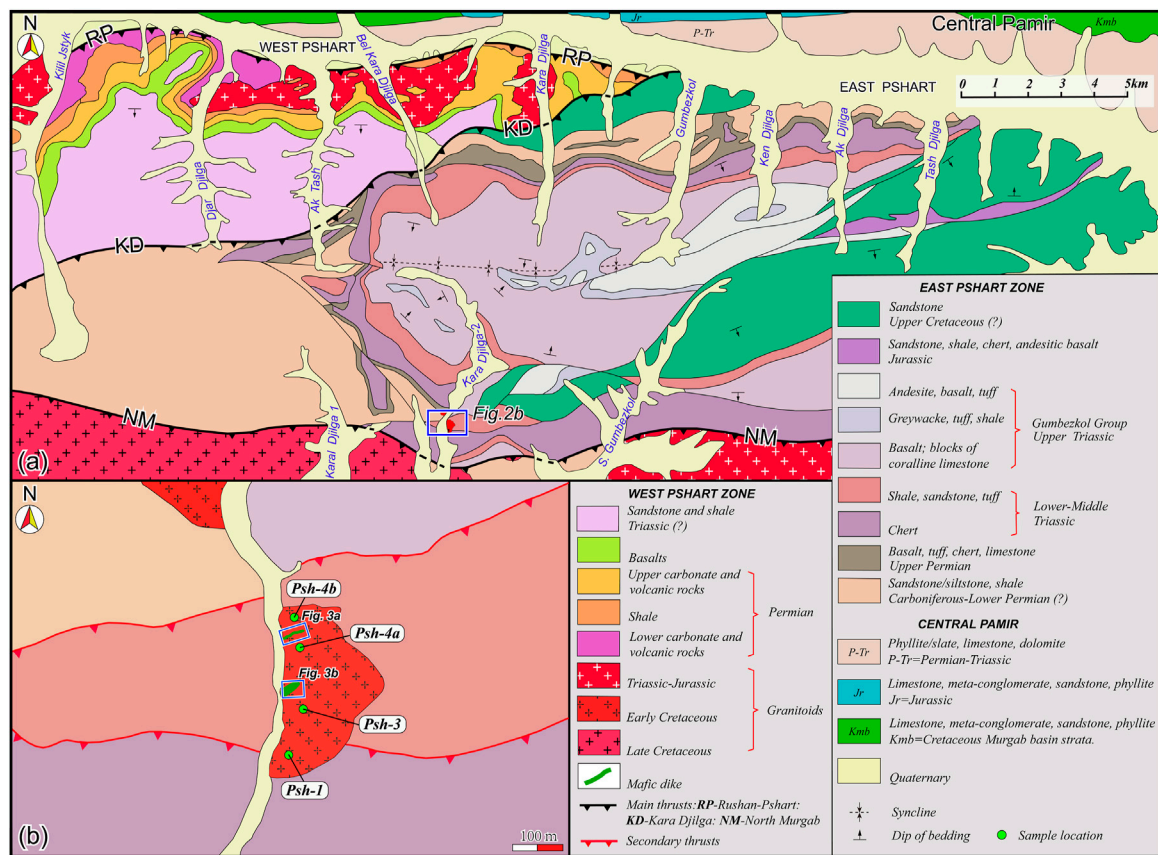
FIGURE 2
(A) Geological map of the Pshart zones showing the Kara Djilga fault, which is the boundary between the East and West Pshart zone. **(B)** Investigation area. The location of **(B)** is shown in **(A)** (red square). The map was modified after Leven (1995).

et al., 2013, 2015; Robinson, 2015; Zanchetta et al., 2018; Wang S. et al., 2020; Villarreal et al., 2020). However, another group argues for the Late Jurassic to Early Cretaceous closure time of the Rushan–Pshart Ocean (Shvol'man, 1978; Pashkov and Shvol'man, 1979; Burtman and Molnar, 1993; Leven, 1995; Schwab et al., 2004; Li R. H. et al., 2019; He et al., 2019; Fan B. et al., 2021). The eastward and westward continuation of the RPSZ also remains uncertain and controversial. Burtman and Samygin (2001); Burtman (2010); Angiolini et al. (2013); Villarreal et al. (2020) and Wang S. et al. (2020) correlated the RPSZ to the Longmu Co-Shuanghu suture zone, which is defined as the boundary between the Northern and Southern Qiantang terrane (Liang et al., 2012; Zhao et al., 2015; Zhai et al., 2016). However, other scholars correlated the RPSZ to the Bangong–Nujiang suture of Tibet (Lacassin et al., 2004; Schwab et al., 2004; Valli et al., 2008; Li R. H. et al., 2019), which separates the Southern Qiantang from Lhasa terrane (Liu et al., 2017; Hu et al., 2019; Wang W. et al., 2020).

Granitic rocks form in different geodynamic settings (Floyd and Winchester, 1975; Pearce and Norry, 1979; Petro et al., 1979;

Pitcher, 1983; Maniar and Piccoli, 1989; Förster et al., 1997), and their proper classification, precise dating, and neat interpretation can be used as a geodynamic indicator of switch in the geodynamic environment (Barbarin, 1999; Dong et al., 2011; Zheng and Gao, 2021). The RPSZ is invaded by the Triassic–Jurassic and Cretaceous granites (the Cretaceous granites are invaded by diabase dikes (Figure 3) (Schwab et al. (2004) and this study)). The relationship of the granites and diabase dikes with the country rocks and their distinct characteristics may reveal the tectonic significance and particular stage of the tectonic evolution of the Pamir Orogen. The mechanism, emplacement timing, nature/protolith, provenance source, and geodynamic significance of the granites and their genetic relationship with diabase dikes and surrounding rocks remain unresolved. This paper, presents the petrographical description, geochronological and geochemical results of Early Cretaceous granites, and geochemistry of diabase dikes along the Kara Djilga-2 valley of the eastern Pshart zone (Figure 2) to reveal their geodynamic significance, nature, and provenance. Based on our observation/results in integration with

previous studies on Pamir, we propose a new model for the tectonic evolution of the Rushan–Pshart Meso-Tethys Ocean during the Mesozoic and its tentative correlations to the eastern and western extensions in the Tibetan Plateau.

2 Geological background

The Pamir orogen is in the western part of the Tibetan Plateau and comprises three extensive E–W-trending suture zones. From north to south, these sutures are the Tanymas Suture Zone (TSZ), the Rushan–Pshart Suture Zone (RPSZ), and the Wakhan–Tirich Boundary Zone (WTSZ) (Figure 1) (Burtman and Molnar, 1993; Zanchi et al., 2000; Burtman, 2010; Zanchi and Gaetani, 2011; Robinson, 2015). These suture zones subdivide the Pamir Plateau, from north to south, into the Northern Pamir/Karakul Mazar (Asian affinity), the Central Pamir, the Southern Pamir, and the Karakoram terranes (Cimmerian blocks) (Burtman and Molnar, 1993; Schwab et al., 2004). To the east and west, it is bounded by the transpressional Karakoram (dextral) and Darvaz (sinistral) faults respectively (Figure 1) (Burtman and Molnar, 1993; Robinson, 2009). The Northern Pamir is a part of the Kunlun Orogen that developed in response to subduction–accretion processes and the consumption of the Tethyan Oceans (Xiao et al., 2002; Robinson et al., 2012; Robinson, 2015; Li Y et al., 2018; Imrecke et al., 2019; Chen et al., 2021). Widespread intermediate granitoids of Triassic age (230–210 Ma) extensively intrude into the meta-sedimentary and meta-igneous mélange of the Karakul–Mazar accretionary complex (Schwab et al., 2004; Robinson et al., 2007). The exposed Late Triassic to Early Jurassic metamorphic rocks along the Karakul–Mazar arc-accretionary complex record the amalgamation process of the Northern and Central Pamir (Qu et al., 2007; Robinson et al., 2007, 2012; Yang et al., 2010; Li Y. P. et al., 2020; Rembe et al., 2021). The Northern Pamir (Karakul–Mazar arc accretionary complex) is considered the western extension (along-strike equivalent) of the Songpan–Ganzi terrane (Yin and Harrison, 2000; Schwab et al., 2004; Robinson et al., 2012; Robinson, 2015; Groppo et al., 2019; He et al., 2019; Imrecke et al., 2019). The structural analysis and proposed models suggest that, before its complete consumption, the Paleo-Tethys started to subduct southward beneath the Central Pamir (Robinson et al., 2012; Robinson, 2015; Imrecke et al., 2019). However, recent studies in the Muztaghata dome contradict this interpretation, assuming that the Gondwana affinity Central Pamir terrane juxtaposed above the Asian affinity Karakul–Mazar terrane during the exhumation of the lower crust in the Miocene, rather than during its southward subduction beneath Central Pamir (Li Y.-P. et al., 2020). The Central Pamir comprises metamorphic domes that mainly consist of marbles and siliciclastic rocks ranging in age from Paleozoic to Mesozoic, which are strongly

folded and subjected to ductile deformation (Schwab et al., 2004; Stearns et al., 2015; Rutte et al., 2017a; 2017b). In the northeastern part of the Central Pamir, Triassic rocks (flysch and sedimentary mélange) of the Karakul–Mazar terrane were thrust to the Central Pamir along the Akbaital–Kalaktash thrust and unconformably overlay the Proterozoic to Cenozoic rocks (He et al., 2019). In the southeastern part, Late Triassic granitoids (206–201 Ma) intruded due to the northward subduction of the Rushan–Pshart Ocean beneath the Central Pamir (Wang S. et al., 2020). The youngest documented Mesozoic igneous rock in the Central Pamir is the Late Cretaceous (74–72 Ma; Figure 1) (Schwab et al., 2004; Chapman et al., 2018b). Chapman et al. (2018b) associated the Late Cretaceous mafic magmatism with the slab rollback of the Neo-Tethyan oceanic lithosphere, causing limited extension in Pamir. The Rushan–Pshart suture zone marks the boundary between the Central and Southern Pamir terranes (Figure 1) (Leven, 1995; Yogibekov et al., 2020), considered to be the western equivalent of the greater Qiantang terrane of the Tibetan Plateau (Burtman and Samygin, 2001; Robinson et al., 2012; Angiolini et al., 2013; Robinson, 2015; Wang S. et al., 2020; Villarreal et al., 2020). The Southern Pamir is divided into the Southeast (SE) and Southwest (SW) Pamirs, based on their different rock assemblages and metamorphic degrees of the exposed rocks.

The SE Pamir comprises non or slightly-metamorphosed mostly sedimentary and igneous rocks that record the tectonic evolution of the SE Pamir from its drifting from Gondwana until its accretion to the southern margin of Eurasia (rift to drift history) (Angiolini et al., 2013, 2015). The SW Pamir comprises the Neogene Alichur and Shakhdara gneiss dome complex, which was exhumed from a depth of 10–15 km (Alichur dome) and 30–55 km (Shakhdara dome) along the Alichur–Gunt and South Pamir sear zones, respectively (Schmidt et al., 2011; Stübner et al., 2013a; 2013b; Stearns et al., 2015; Worthington et al., 2020). The boundary between the Southern Pamir and Karakoram terrane is defined by the WTBZ, along which serpentinized mantle peridotites are exposed (Zanchi et al., 2000; Zanchi and Gaetani, 2011). Within the Southern Pamir, the exposed ophiolites in the hanging wall of the Alichur dome have been interpreted as the obducted fragment of the Rushan–Pshart oceanic lithosphere (north Alichur and Bashgumbaz ophiolites) (Shvol'man, 1980). However, a recent study on the Bashgumbaz complex revealed that the ophiolites formed in a supra-subduction setting during the initial southward subduction of the Rushan–Pshart Ocean beneath the Southern Pamir (Zanchetta et al., 2018). Liu et al. (2020c) first documented the Late Triassic–Early Jurassic monzogranite of 202–197 Ma (Turuke pluton) in the Southern Pamir. The Early and Late Cretaceous rocks intruded into the basement of the southern Pamir. To the south, the Shyok suture may have formed as a result of an amalgamation of the Kohistan–Ladakh intra-

oceanic arc and Karakoram terrane by the Late Cretaceous (Ravikant et al., 2009; Pundir et al., 2020; Saktura et al., 2021).

2.1 The geology of the Pshart zones

The Rushan–Pshart suture zone was considered a separate zone from the Central and Southern Pamirs by Dronov (1964). This zone comprises three distinct lens-shaped blocks (Rushan, Pshart, and Dunkeldyk) (Figure 1). Two distinct zones were distinguished within the Pshart zone and the Eastern and Western Pshart zones, which are separated by the Kara–Djilga fault (Figure 2A) (Pashkov and Shvol'man, 1979; Leven, 1995). The geology of the Rushan and Dunkeldyk blocks was briefly described by Leven (1995) and Zanchetta et al. (2018). The Pshart complex is the focus of the present study.

2.1.1 Western Pshart

The Western Pshart zone starts with the massive succession of the carbonate, shale, and interlayer volcanic rocks Permian in age, which were locally intruded by Late Triassic–Jurassic granitoids. The lithology is locally strongly metamorphosed and deformed by multiple faults. The presence of the alkaline picritic basalt was interpreted to be associated with the initial stage of the rifting and opening of the Rushan–Pshart Ocean (Pashkov and Shvol'man, 1979; Leven, 1995). Basalt, andesitic basalt, and basic effusive rocks with subordinating basic and acidic tuffs and local thin layers of clayey-shale and embedded fragments of the limestone occur in the intermediate part of the succession. The upper section mostly consists of volcaniclastic sandstone, shale, and siltstone, with distinctive layers of altered basalt and intermediate to acidic tuffs (about 10 m) of undetermined ages (Pashkov and Shvol'man, 1979; Leven, 1995). For more detailed information, refer to Leven (1995).

2.1.2 Eastern Pshart

The Eastern Pshart zone is characterized by Carboniferous to Permian clastic rocks, followed upward by volcaniclastic limestones and basalt of Upper Permian age (Leven, 1995). However, recent investigations revealed that it is a sedimentary mélange, comprising incorporated fragments of the upper portion of oceanic plate stratigraphy (OPS), with Upper Triassic (212 Ma) maximum deposition age (MDA), rather than Carboniferous or Permian (Yogibekov et al., 2020). Following upward, the Triassic interval is represented by Upper Triassic volcanic and sedimentary deposits (Gumbezkol Group; up to 1000 m) overlying chert, shale, and sandstone with layers of andesite and basalt of Lower to Middle Triassic age. The Upper Triassic Gumbezkol group comprises basalt and embedded blocks of limestone in the lower part, passing upward to clastic rocks such as greywacke, alternating with andesitic tuff, silicious shale, conglomerate, and breccia. The upper portion comprises andesite, andesitic basalt, and tuff.

Small amounts of spilite, basalt, and diabase with thin layers of chert, limestone, shale, and tuffitic sandstone also occur. Late Triassic age was tentatively inferred for the section based on its stratigraphic position and poorly dated fossils (Leven, 1995). The Upper Jurassic and Cretaceous rocks (Etchki Tushar Formation) are composed of andesite, andesitic basalt and tuff, limestone, and sandstone, together with chert and/or cherty-shale (Pashkov and Shvol'man, 1979; Leven, 1995). The non-conforming overlying sandstone was tentatively dated as the Late Cretaceous (Leven, 1995).

3 Sampling and petrography

We collected four granite (Figure 2B) and two diabase (Figures 3A,B) samples, which cropped out in the southern part of the eastern Pshart zone, along the Kara Djilga-2 River (Figure 2B). The granitic rocks intruded into Early–Middle Triassic rocks, composed of shale, sandstone, tuff (Figures 2A,B), and cherty units, showing sharp intrusive contact (Figure 3C). The basic rocks occurred as diabase dikes (ranging in size from 50 cm up to 10 m), which invaded the granitic rocks (Figures 3A,B). Thin sections were made by Beijing GeoAnalysis Technology Co., Ltd. We classified the granitic rocks as two-mica monzogranite based on our microscopic observation. The granitic rocks were medium-to-fine-grained and contained plagioclase (40%), K-feldspar (30%), quartz (25%), biotite, and muscovite (≤5%), as well small amounts of garnet and accessory minerals, such as apatite and zircon (Figures 3E,F). The plagioclase was semi-automorphic in shape, with twining crystal development, and moderately subjected to sericitization. Occasionally, the plagioclase fractured, and quartz veins filled the cracks. The K-feldspar was slightly muddy with a striped feldspar structure. The diabase was represented by samples Psh-6 and Psh-7, which predominantly consisted of plagioclase (50%), pyroxene (35%), amphibole (10%), and olivine (5%) (Figure 3D). Apatite, magnetite, and titanomagnetite were present as accessory minerals. Disordered plagioclase was distributed within the rock and slightly altered to kaolinite and sericite, representing the matrix within the rocks. Micro-fissures were also observed in the diabase. The interstices were filled with carbonate and quartz veins.

4 Results

4.1 Geochronology

The detailed analytical methods are provided in Supplementary Material. Zircon grains from the granitic rocks including samples Psh-1, Psh-3, Psh-4a, and Psh-4b from the Kara Djilga-2 section were subjected to LA-ICP-MS U-Pb zircon
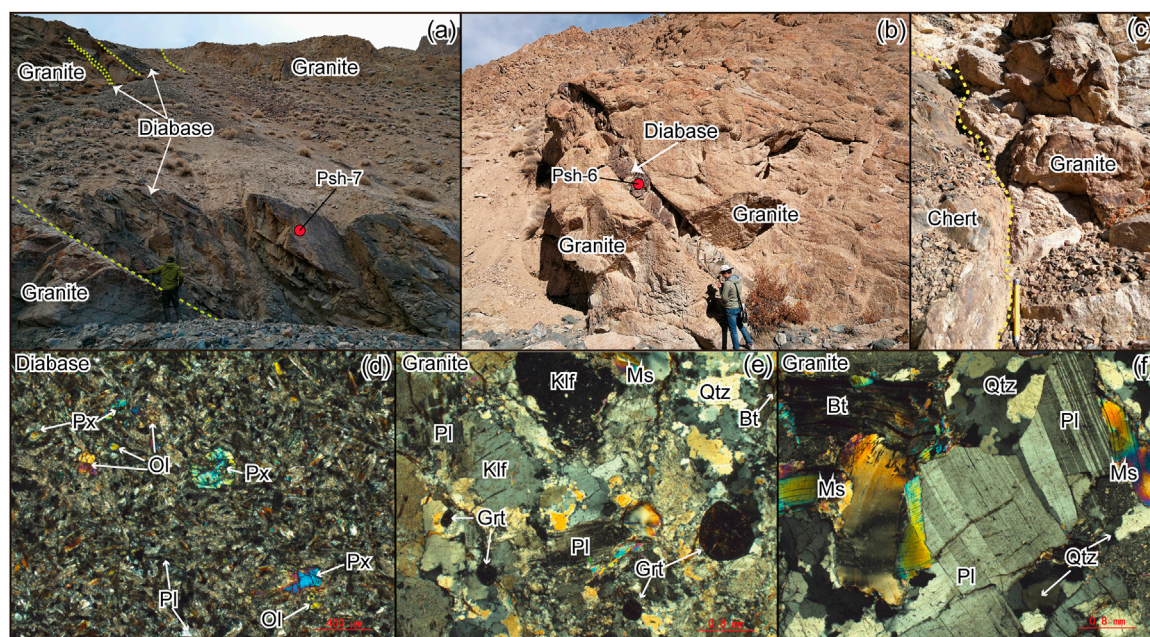
FIGURE 3
(A,B) Variably sized diabase dikes intruding into the granitic rocks. Their location is shown in Figure 2B. Scientists for scale. **(C)** Intrusion contacts between chert and invaded granite. **(D)** Photomicrograph of diabase rocks, the location of which is shown in Figure 2B. **(E,F)** Photomicrographs of granites. Px, pyroxene; Ol, olivine; Pl, plagioclase; Kfl, K-feldspar; Ms, muscovite; Bt, biotite; Qtz, quartz; Grt, garnet.

dating to determine the crystallization age and intrusion time of the granitic magma. We utilized the Th/U ratio (Corfu et al., 2003) to distinguish the genetic origins of the zircons as either metamorphic or igneous growth. The zircon crystals from the samples varied in color from colorless, deep black, and grayish. They were euhedral, subhedral, and tabular in shape. Most of the zircons showed well-developed oscillatory zoning with a lack of core and rim structure in cathodoluminescent images (Figure 4F). The zircon grains ranged in length from 60 to 190 µm, with variable concentrations of Th (51–1439) and U (87–4053) that yielded Th/U values of 0.16–0.97 (only a few spots yielded ratios of 0.06–0.07), consistent with a magmatic origin (Corfu et al., 2003). The U-Pb systematics are provided in Supplementary Table S1.

The data from Psh-1 yielded ^{206}Pb/^{238}U ages ranging from 116 to 130 Ma and a weighted mean age of 121.9 ± 2.6 Ma (MSWD=4.3, n=12; Figure 4A). Three grains yielded older ages, ranging from 136 to 137 Ma, with a weighted mean age of 135.9 ± 24 (Figure 4A). However, these zircons were slightly discordant; thus, we did not consider them in the crystallization aging.

Eleven analyses from sample Psh-3 showed ^{206}Pb/^{238}U ages ranging from 107 to 123, with a weighted mean age of 118.0 ± 2.5 Ma (MSWD = 3.6, n = 11; Figure 4B). Three zircons from sample Psh-4a yielded ages ranging from 113 to 128 Ma with a weighted mean ^{206}Pb/^{238}U age of 122.9 ± 4.8 Ma (MSWD = 11, n = 10; Figure 4C). Two inherited zircon crystals showed ages of

180 ± 2 and 877 ± 4 Ma from the same sample, with Th concentrations of 51–85 ppm, U concentrations of 87–921ppm, and Th/U of 0.05–0.87 (Figure 4C).

Zircon crystals from sample Psh-4b ranged in age from 112 to 131 Ma, with a weighted mean ^{206}Pb/^{238}U age of 124.5 ± 2.0 Ma (MSWD = 3.6, n = 16; Figure 4D). A single inherited zircon grain of 924 ± 5 Ma was obtained from the sample. The weighted mean ages were interpreted as the crystallization age for each sample.

Zircons from the diabase sample Psh-7 yielded only Precambrian concordant ages and were not further considered (Supplementary Table S1). Similarly, the diabase Psh-6 yielded mostly inherited Precambrian ages, with single concordia age of 121 Ma with a Th/U ratio of 0.49, indicating the magmatic origin of the zircon (Figure 4E).

4.2 Geochemistry

4.2.1 Geochemistry of the granites

The major and trace element compositions of the granite samples are shown in Supplementary Table S2. The granitic rocks showed loss on ignition (LOI) values of 1.03 wt.% to 1.42 wt.%, while those of diabases were 1.14 wt.% and 8 wt.%, indicating the relative freshness of the samples except for Psh-7, which showed a high LOI. The granites were characterized by high SiO$_2$
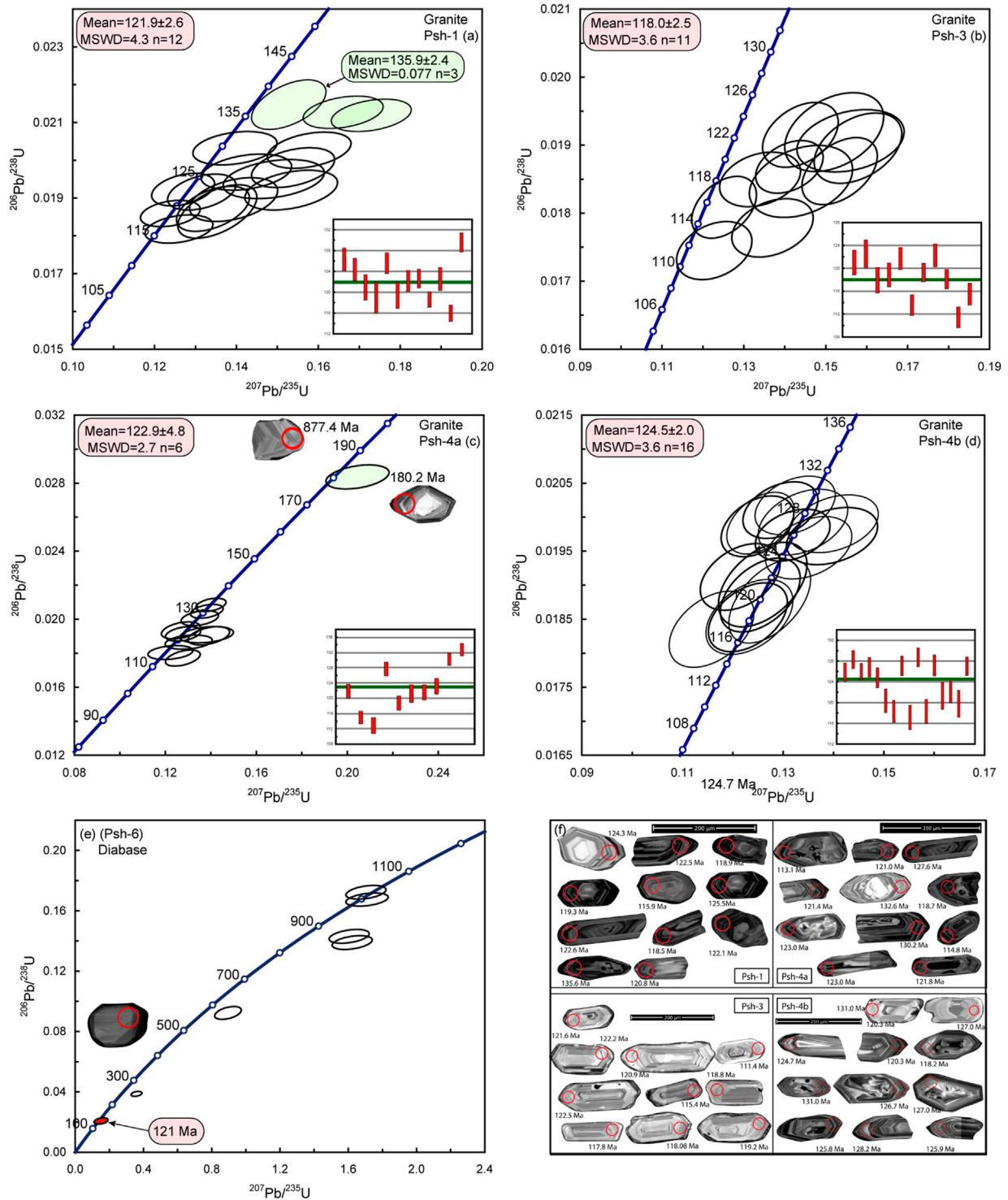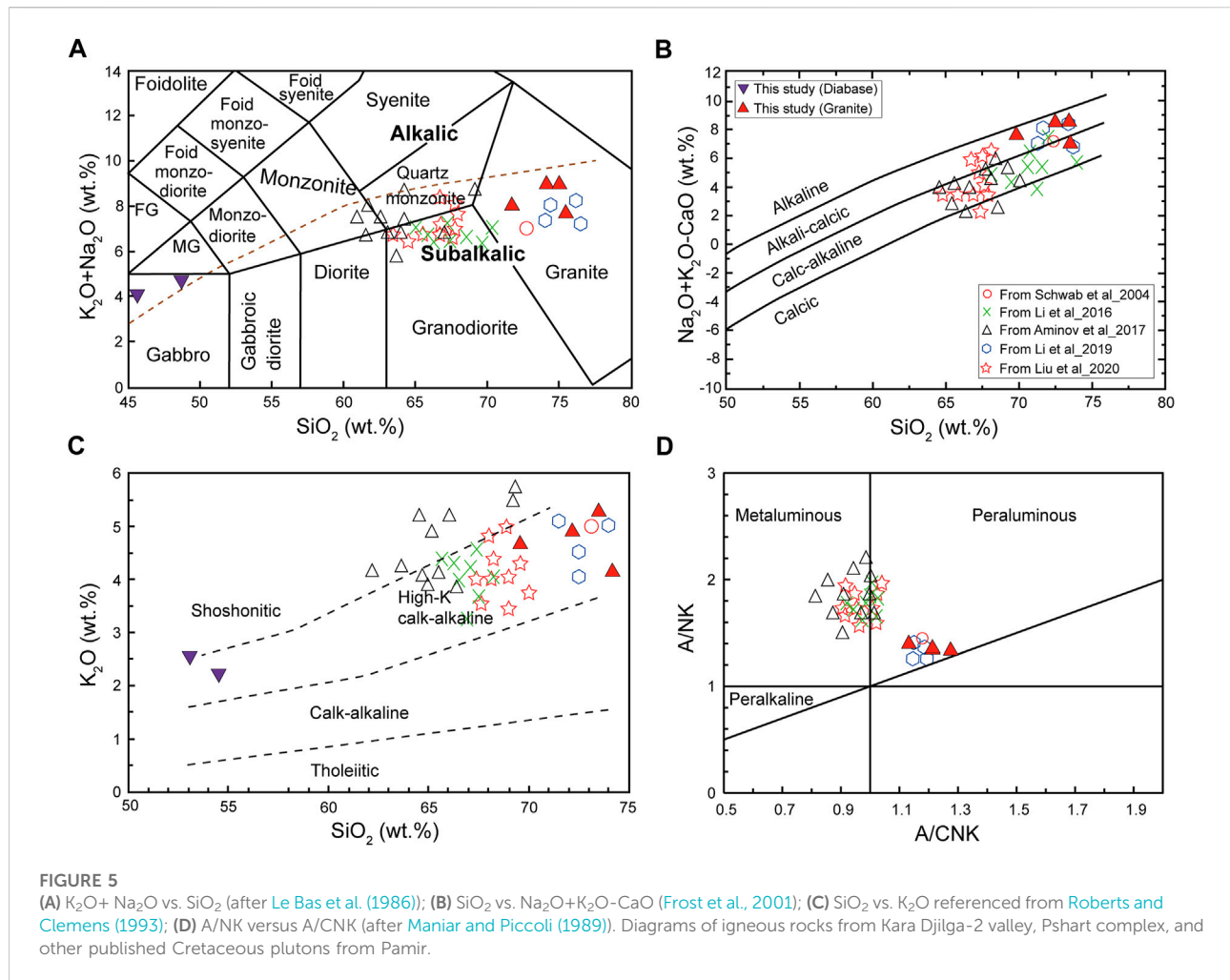
FIGURE 4
(A–D) U–Pb Concordia diagrams of zircons from granites. (E) Diabase dike and (F) CL images of dated granite zircons. MSWD, mean square of the weighted deviation.

FIGURE 5
(A) K$_2$O+ Na$_2$O vs. SiO$_2$ (after Le Bas et al. (1986)); **(B)** SiO$_2$ vs. Na$_2$O+K$_2$O-CaO (Frost et al., 2001); **(C)** SiO$_2$ vs. K$_2$O referenced from Roberts and Clemens (1993); **(D)** A/NK versus A/CNK (after Maniar and Piccoli (1989)). Diagrams of igneous rocks from Kara Djilga-2 valley, Pshart complex, and other published Cretaceous plutons from Pamir.

concentrations ranging from 70.32 to 74.40 (wt.%), with total alkali (Na$_2$O+K$_2$O) ranging from 7.69 wt.% to 8.96 wt.%. In the SiO$_2$ vs. K$_2$O+Na$_2$O diagram of Le Bas et al. (1986), the samples were classified as granitic rocks, consistent with our microscopic observations (Figure 5A).
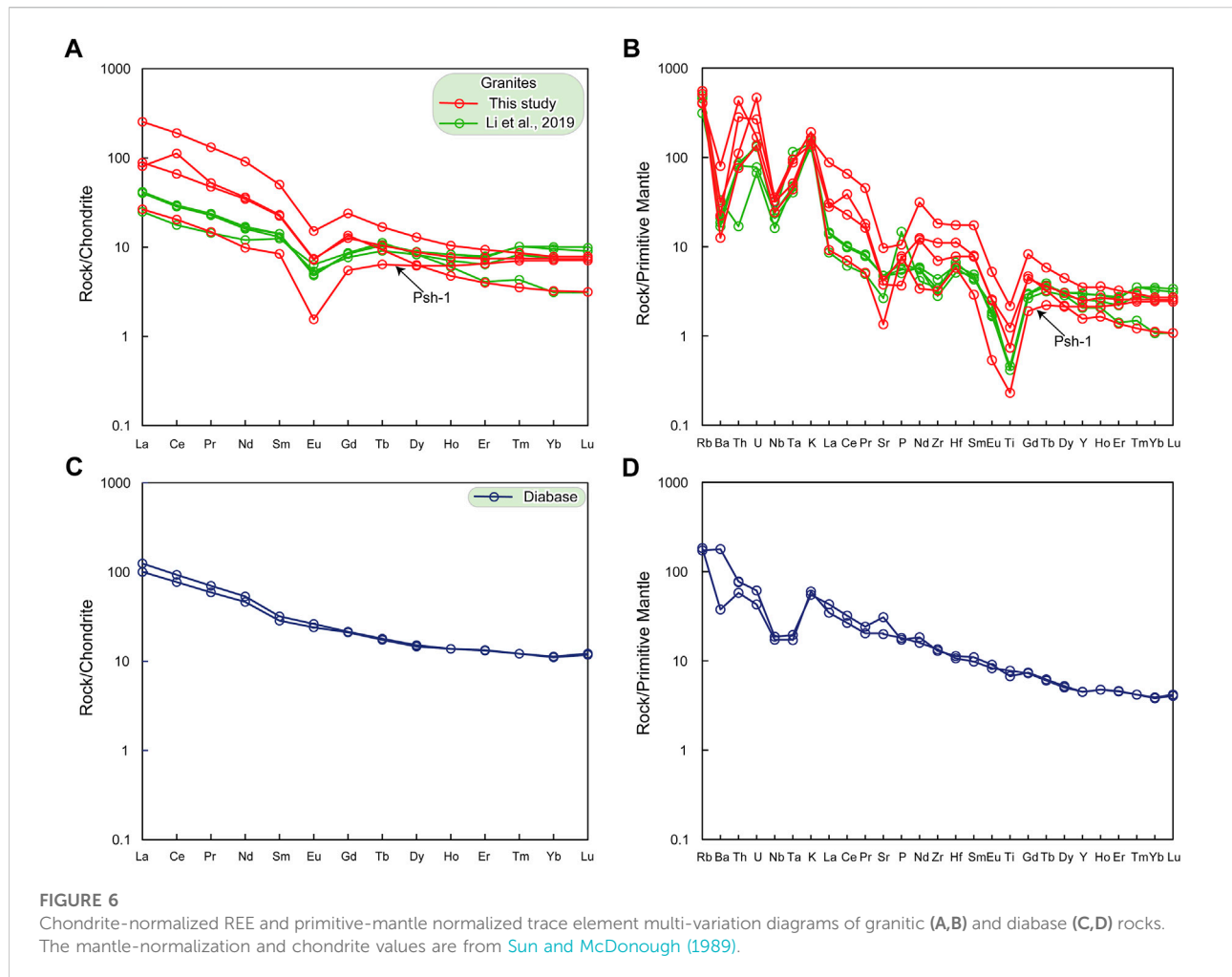
K$_2$O ranged from 4.21 wt.% to 5.79 wt.%, CaO from 8.54 wt.% to 8.55 wt.%, and Na$_2$O from 3.17 wt.% to 3.95 wt.%, with K$_2$O/Na$_2$O ratios of 1.21–1.83 and CaO/Na$_2$O ratios of 0.03–0.44. In the SiO$_2$ vs. Na$_2$O+K$_2$O-CaO (wt.%) and SiO$_2$ vs. K$_2$O classification diagrams, the granites plotted in the field of calc-alkaline to alkali-calcic and high-K calc-alkaline series, respectively (Figures 5B,C). The granitic rocks were similar to S-type granitoids, with strongly peraluminous features (Figure 5D) and high alumina saturated indexes (ASI) of A/CNK (Al$_2$O$_3$/(CaO+Na$_2$O +K$_2$O) $_{mol}$.) and A/NK (Al/Na$_2$O +K$_2$O) $_{mol}$.), ranging from 1.13 to 1.28 and 1.21 to 1.83, respectively. The samples showed moderate concentrations of Al$_2$O$_3$, ranging from 13.49 to 15.53, and low TiO$_2$ content, ranging from 0.05–0.47, with Al$_2$O$_3$/TiO$_2$ ratios ranging from 31.43 to 310.06. They were also characterized by varying content

of Fe$_2$O$_3$^{T} (0.48–2.81) and CaO (0.12–1.42) and low MgO (0.13–0.87), with Mg# between 26.3 and 46.4.

In the chondrite-normalized patterns, the granitic samples showed light rare earth element (LREE) enrichment relative to heavy rare earth elements (HREE, La$_N$/Yb$_N$ = 3.73–32.58) with strong depletion of Eu (Eu/Eu* = 0.22–0.41; (Figure 6A)). In the primitive normalized spidergram, the samples showed strong depletion of Ba, Sr, Eu, and Ti and a comparatively weak negative Nb anomaly. The samples showed variable enrichment on Th, U, and K and strong enrichment of Rb (Figure 6B). The depletion of Sr and Eu likely reflected plagioclase fractionation or accumulation, consistent with our petrographical observations (Figures 3E,F).

4.2.2 Geochemistry of the diabase dikes

The diabase dike samples (Psh-6 and Psh-7) showed relatively low SiO$_2$ content, ranging from 49.77 to 50.71. The K$_2$O content ranged from 1.66 wt.% to 1.80 wt.%, while Na$_2$O ranged from 2.84 wt.% to 3.22 wt.%, with the K$_2$O/Na$_2$O ratios ranging from 0.51 to 0.63. The Al$_2$O$_3$ content ranged from

FIGURE 6
Chondrite-normalized REE and primitive-mantle normalized trace element multi-variation diagrams of granitic **(A,B)** and diabase **(C,D)** rocks. The mantle-normalization and chondrite values are from Sun and McDonough (1989).

16.15 wt.% to 16.95 wt.%. The TiO_2 content was slightly high (1.46 wt.% to 1.48 wt.%). The Fe_2O_3 content was 8.73–9.48 wt.%, and high MgO content was also observed, ranging between 7.93 and 8.58 wt.%, with Mg# between 62.4 and 66.1. The samples plotted in the gabbroic field and showed alkaline affinity in the TAS diagram (Figure 5A). In the SiO_2 vs. Na_2O+K_2O diagram, the samples plotted in the alkaline series field (Supplementary Figure S2B). In the SiO_2 vs. K_2O classification diagram, the samples fell in the high-K calc-alkaline and shoshonitic rock series (Figure 5C). The Nb, Yb, and Th content ranged from 12.3–13.3 ppm, 1.88–1.92 ppm, and 4.92–6.59 ppm, respectively, with Nb/Yb and Th/Yb ratios of 6.54–6.93 to 3.43–2.6.

In the chondrite-normalized REE diagrams (Sun and McDonough, 1989) the samples were characterized by LREE enrichment compared to HREEs, which displayed relatively flat patterns without Eu anomalies (Figure 6C). In the multi-elemental spidergram (Sun and McDonough, 1989), the samples showed depletion of high-field strength elements (Nb and Ta), with negligible positive Sr and Ti anomalies. Slightly positive and negative Ba anomalies were also observed (Figure 6D).

5 Discussion

5.1 Petrogenesis

5.1.1 Granite

The granites were high-K calc-alkaline with high SiO_2 content [70.32–74.40 (wt.%)], strongly peraluminous (A/CNK=1.13–1.28), with K_2O/Na_2O ratios ranging from 1.21 to 1.83, suggesting that they were strongly peraluminous S-type granites (Chappell and White, 1992; Patiño Douce and Harris, 1998; Chappell, 1999; Clemens, 2003; Clarke, 2019; Liu X. et al., 2021). These findings are also supported by the A/CNK vs. SiO_2 diagram (Figure 7A). The results of multi-experimental studies revealed that most of the S-type granites formed from the partial melting of metasedimentary rocks (Chappell and White, 1974; Beard et al., 1993; Clemens, 2003; Stevens et al., 2007; Wang et al.,

2007; Villaros et al., 2009b; Bartoli et al., 2013; Champion and Bultitude, 2013; Wang et al., 2014; Gao et al., 2016b; Gao et al., 2017; Zhu et al., 2018; Clemens et al., 2020; Zhu et al., 2020). The A/CNK ratio can be used to define the boundary between S and I-type granite (Chappell and White, 1974). The A/CNK ratios of S and I-type granites range from 1.044–1.248 and 0.902–1.092, respectively (Chappell, 1999). Our petrographic observations showed the presence of biotite, muscovite, and garnet and the absence of mafic phase minerals, suggesting its S-type nature (Chappell and White, 1992; Villaros et al., 2009a). The high K_2O (4.21–5.79) content relative to Na_2O (3.17–3.95), with K_2O/Na_2O values of 1.21–1.83 (Supplementary Table S2), also confirmed that the granites from this study were S-type in nature (Chappell and White, 2001). In the K_2O/MgO vs. 10000*Ga/Al and FeO^T/MgO vs. 10000*Ga/Al diagrams, the samples clearly plotted in the A-type granite field (Figures 7C,E). However, in the K_2O+Na_2O, FeO^T/MgO, (K_2O+Na_2O)/CaO vs. Zr+Nb+Ce+Y diagrams, the samples plotted in the highly fractionated S-type to A-type, highly fractionated S-type to unfractionated I-S-type and highly fractionated S-type, and unfractionated I-S-type, respectively (Figures 7B,D,F). The 10000*Ga/Al value of the samples ranged from 2.79 to 3.52 and Zr+Nb+Ce+Y are 76–359 ppm, which was nearly identical to those of A-type granites, which are characterized by an average 10000 Ga/Al value >2.6 and Zr+Nb+Ce+Y >350 ppm. However, Whalen et al. (1987) reported that some strongly fractionated S-and I-type granites also show high Ga/Al ratios, thus showing similar characteristics to those of A-type granites. This ambiguity is controlled by the entrainment of xenocrystic/or peritectic and accessory minerals and their constituent element concentrations in the melt. In combination with our data, we used the data from 118 Ma granitoids reported by Li R. H. et al. (2019) (from the Taxkorgan region (Figure 1)), which plotted in the same fields as our samples (Figure 7D). Garnet containing elements such as Zr, Ce, Ga, Y, and others can be concentrated within refractory minerals such as zircon (Zr, Hf, Y, and Yb) and monazite (Ce and La) (Villaros et al., 2009b). Thus, the zircon, monazite, and garnet and their constituent elements may have provided the A-type characteristics in the granite samples in this study. The lack of monazite may be due to its full dissolution and equilibration within the melt, thus changing the compositional variation of the melt (Villaros et al., 2009b; Clemens and Stevens, 2012). These findings imply that the assent of the melt was not rapid after partial melting and segregation of the melt from the magma source rocks and that entrained peritectic and accessory minerals had enough time to dissolve and equilibrate within the melt. The process was well-described by Villaros et al. (2009b). Thus, the dissolution of the peritectic and accessory minerals (equilibrium melting) may have modified the trace element composition of the studied granites. Extremally negative Eu anomalies (Eu/Eu*<0.30) were interpreted to be characteristic of A-type granite (Zhang Q. et al., 2012). However, our samples

displayed comparatively high Eu/Eu* values (0.40–0.42), characterizing them as S-type granite. An exception was sample Psh-1 which showed a slightly lower Eu/Eu* value (0.22). Metasedimentary-derived, highly fractionated S-type granites with geochemical characteristics overlapping those of A-type granites have been reported worldwide (Whalen et al., 1987; Huang and Jiang, 2014; Zhu et al., 2020). The overlap of geochemical characteristics is attributed to the entrainment of peritectic and accessory minerals and their constituent elements, which is in good agreement and can be attributed to our samples. A-type granites are ferroan/and or alkaline in nature (Whalen et al., 1987; Gao et al., 2016b); however, our samples tend to be magnesian and sub-alkaline in the SiO_2 vs. ^TFeO/(^TFeO+MgO) and SiO_2 vs. Na_2O+K_2O diagrams, respectively (Supplementary Figure S2A,B). The negative Eu and Sr anomalies may have been related to the separation of plagioclase from the melt during fractional crystallization or may indicate that the granitic melt was generated in the plagioclase stability field (Figures 6A,B). K-feldspar fractionation was also reflected by the negative Ba and Eu anomalies (Figures 6A,B). The strong negative Ti anomaly reflected the fractionation of ilmenite (Fe–Ti oxides) or mica fractionation during magma evolution. However, the samples showed low Sr/Y and relatively high La/Yb, indicating that the melt was forming in the plagioclase stability field, with residues of garnet and plagioclase (Figures 3E,F), similar to those documented in Jurassic (160 Ma) Maofengshan (South China Block) metasedimentary-derived highly fractionated S-type granites that originated in the middle crust (16.5–20 km) (Liu X. et al., 2021). The chondrite-normalized and spidergram patterns showed that our samples were slightly evolved compared to those reported by Li R. H. et al. (2019) from the Taxkorgan region. The exception was sample Psh-1 which displayed an identical pattern to those for the Taxkorgan granites (Figures 6A,B). Thus, the samples in this study were highly fractionated, strongly peraluminous S-type granites.

The strongly fractionated peraluminous I-type granites showed a nearly identical geochemical signature to those of peraluminous S-type granites (with some overlap) (Miller, 1985; Gao et al., 2016a). We aimed to identify the source protolith of the granites by using their major and trace elements to discriminate between metasedimentary or metaigneous-derived granitic melt. The Th/Sm vs. Th/Yb, Th/Ce vs. Y, and SiO_2 vs. Rb diagrams showed the sediment-derived trends for the melt (Figures 8A–D). Furthermore, the samples showed variable Rb/Ba (0.46–3.73), Rb/Sr (1.3–11.5), CaO/Na_2O (0.04–0.45), and Al_2O_3/TiO_2 (31.43–310.60) ratios and fell within the fields of pelite-derived magmas. The exception was sample Psh-3, which showed a psammite-derived magma source (Figures 9A,B).

Another convincing argument for the metasedimentary-derived melt is the major oxide element magma source discrimination diagrams of Al_2O_3/(FeO^T+Mg+TiO_2) vs. Al_2O_3+FeO^T+MgO+TiO_2 (wt.%) and CaO/
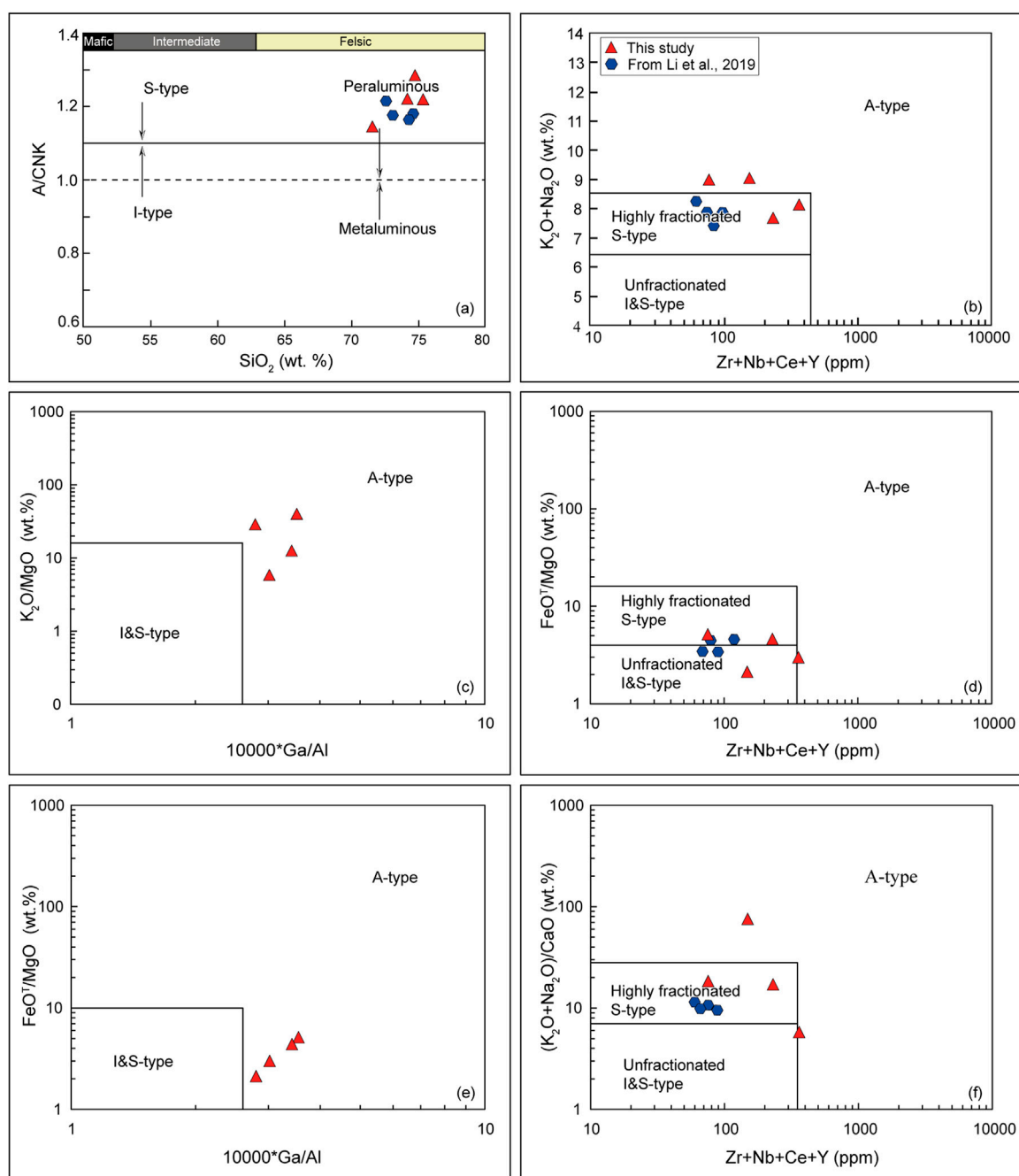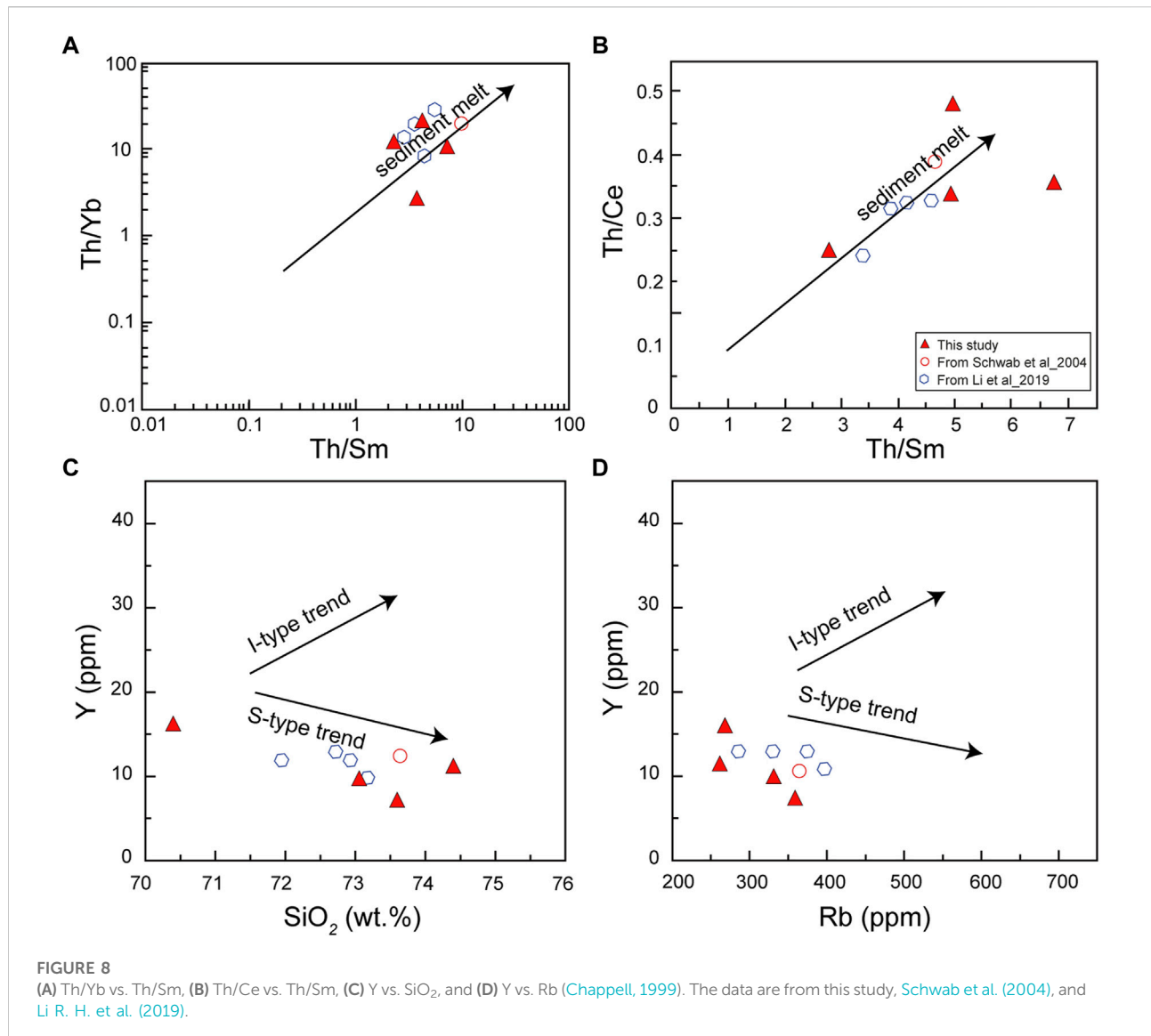
FIGURE 7
(A) A/CNK (molar Al_2O_3/($CaO+Na_2O+K_2O$)) versus Si_2O (after Maniar and Piccoli (1989)). (C,E) K_2O/MgO and FeO^T/MgO vs. 10000*Ga/Al.
(B,D,F) K_2O+Na_2O, FeO^T/MgO and (K_2O+Na_2O)/CaO vs. Zr+Nb+Ce+Y (Whalen et al., 1987).

($MgO+FeO^T+TiO_2$) vs. $CaO+MgO+FeO^T+TiO_2$ (wt.%) (Figures 9C,D). The samples fell in the field of the pelite-derived melt, except for sample Psh-3, which fell in the greywacke field (Figures 9C,D). Based on the major and trace element concentrations, we concluded that the granites originated from the partial melting of metasedimentary rocks

[predominantly from pelite with a minor contribution from psammite (sample Psh-3)] in the plagioclase stability field (middle crust; ±20 km), underwent subsequent fractional crystallization during magma ascent, and were emplaced to the upper crust. We have also compiled available data on Early Cretaceous arc-related and S-type granites and plotted them in
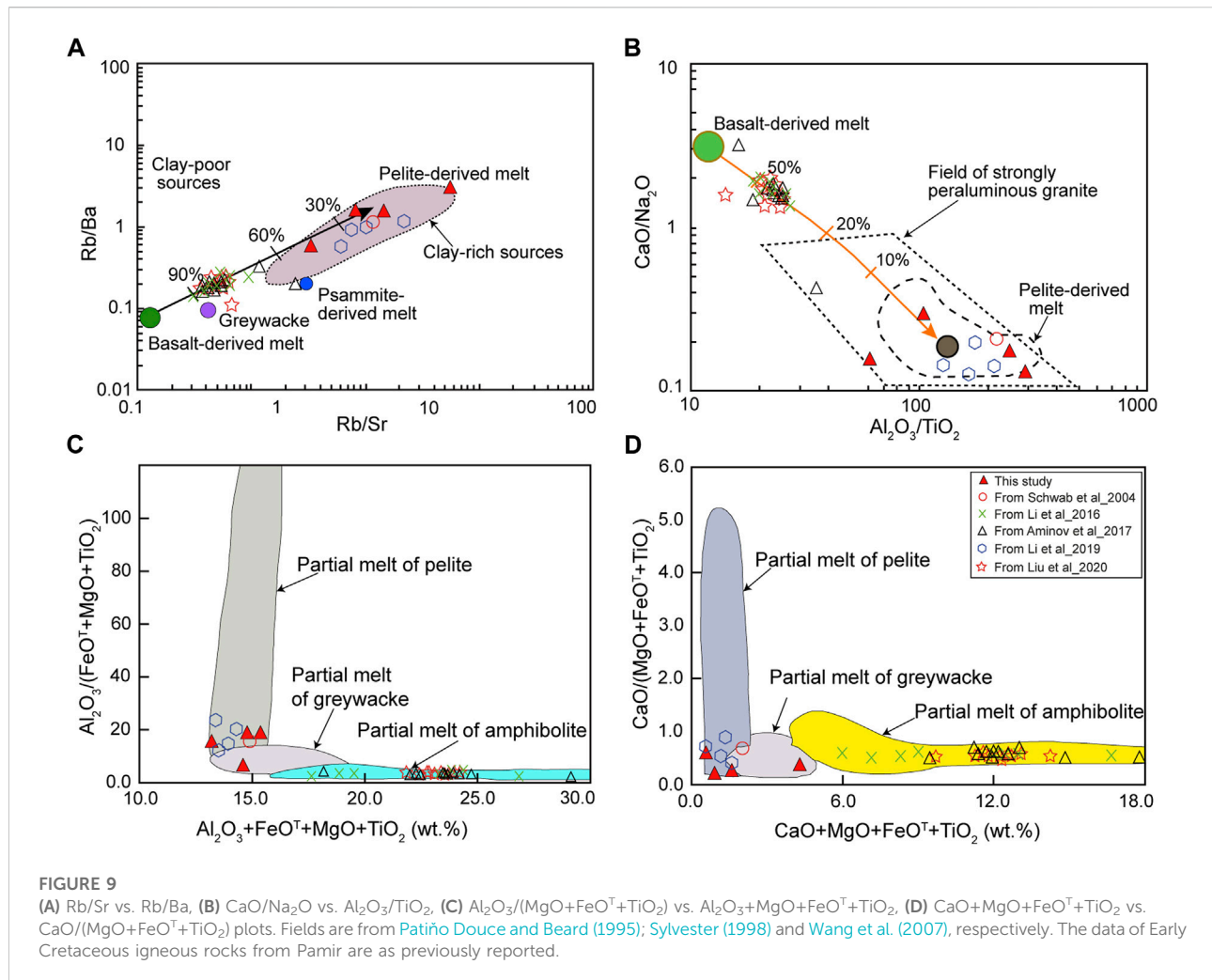
FIGURE 8
(A) Th/Yb vs. Th/Sm, **(B)** Th/Ce vs. Th/Sm, **(C)** Y vs. SiO$_2$, and **(D)** Y vs. Rb (Chappell, 1999). The data are from this study, Schwab et al. (2004), and Li R. H. et al. (2019).

combination with our samples (Figures 5, 8, 9). The arc-related igneous rocks show an obviously different trend.

5.1.2 Mafic dikes

The diabase samples showed a low SiO$_2$ content (49.77–50.71 wt. %) and high MgO (7.93–8.58), Fe$_2$O$_3^T$, Cr (220–300), and Mg# (62.4–66.1) contents, indicating that the mantle-derived parental melt was not evolved, as also suggested by their trace element concentration in the primitive mantle and chondrite-normalized multi-elemental diagram (Figures 6C,D). The moderate-to-high loss on ignition (LOI) value (1.14–8 wt.%) indicated that the samples had undergone variable degrees of alteration. The samples showed a large range in TiO$_2$ content (1.46–1.68 wt.%), which was interpreted as a typical feature of ocean island basalt (OIB)/or oceanic plateau and continental

flood basalt (CFB), associated with the hot-spot zone/or plume activity. However, they are typically hump-shaped in pattern with positive Nb and Ta anomalies in trace element spidergrams (Safonova et al., 2009; Xia, 2014; Xia and Li, 2019). The depletion of Nb and Ta resulted in a continental crust or arc-like signature to the mafic dikes, reflecting the metasomatism of the source region (Donnely et al., 2004). Their crustal or arc-like signature was inherited from the foundering of the Rushan–Pshart oceanic lithospheric crust, which released the fluid-like component and fertilized the overlying mantle (Figure 10). Contamination by crustal rocks may also imprint such a signature. The inherited Precambrian zircons (Figure 4E and Supplementary Figure S1) support crustal contamination. Both crustal contamination and metasomatism can cause Nb and Ta negative anomalies. A simple way to explain the slightly high TiO$_2$ concentration of

FIGURE 9
(A) Rb/Sr vs. Rb/Ba, **(B)** CaO/Na$_2$O vs. Al$_2$O$_3$/TiO$_2$, **(C)** Al$_2$O$_3$/(MgO+FeO^T+TiO$_2$) vs. Al$_2$O$_3$+MgO+FeO^T+TiO$_2$, **(D)** CaO+MgO+FeO^T+TiO$_2$ vs. CaO/(MgO+FeO^T+TiO$_2$) plots. Fields are from Patiňo Douce and Beard (1995); Sylvester (1998) and Wang et al. (2007), respectively. The data of Early Cretaceous igneous rocks from Pamir are as previously reported.
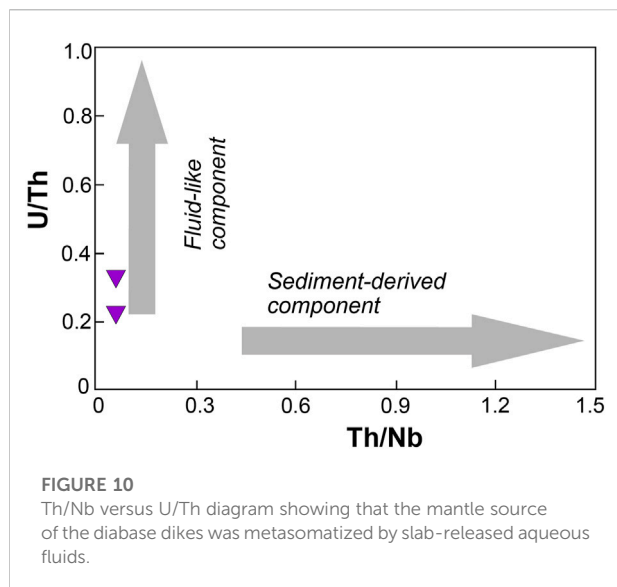
the diabase dikes is that it was inherited and coupled with the opening of the Rushan–Pshart Ocean in the Permian, which has been interpreted to be associated with the plume-related magmatism, as evidenced by high TiO$_2$ content of the basaltic rock of the West Pshart and SE Pamir (Pashkov and Shvol'man, 1979; Tadjidinov, 1988; Leven, 1995; Angiolini et al., 2015). Thus, the upwelling of mafic magmatism and melting of the former TiO$_2$-rich subcontinental lithospheric mantle or crust caused TiO$_2$ enrichment of the diabase dikes. Fractional crystallization/ or accumulation of plagioclase causes strong depletion of melt on Sr and Eu. However, in the primitive mantle-normalized trace-element diagram, the samples did not show any Eu anomaly, with a slightly positive Sr anomaly (Figure 6C). Thus, the lack of Eu anomaly was ascribed to plagioclase-free assemblage at >40 km depth of the lower crust source (Girardi et al., 2012). The slightly positive and negative Ba anomaly was probably the effect of the continental crust contamination/or alteration, which is also supported by the high LOI and inherited zircons in the samples (Supplementary Table S1). Based on the geochemical

data, we proposed that the parental magma of the diabase dikes possibly originated from depleted mantle sources, which may have been metasomatized by fluids released from the detached Rushan–Pshart oceanic lithospheric slab and its foundering in the Late Jurassic–Early Cretaceous. This interpretation is also supported by the U/Th and Th/Nb diagrams, which showed the involvement of fluid-like components in the generation of the parental magma of the diabase dikes (Figure 10).

5.2 Geodynamic settings

5.2.1 Granites

Peraluminous granitoids might form during crustal thickening following the final ocean closure in the continent–continent collisional phase, along shear zones (or along strike–slip faults). In addition, the delamination of the lower crust/of former oceanic crust can cause upwelling of the asthenospheric mantle and its underplating, which serves as a

FIGURE 10
Th/Nb versus U/Th diagram showing that the mantle source of the diabase dikes was metasomatized by slab-released aqueous fluids.

heat source to generate granitic melt by partial melting of infracrustal and supracrustal rocks (Harris et al., 1986; Barbarin, 1996, 1999; Sylvester, 1998; Reichardt and Weinberg, 2012; Huang et al., 2015; Chen Y.-X. et al., 2017; Liu X. et al., 2021; Zheng and Gao, 2021). Based on the aforementioned discussion, we defined the granites as high-K calc-alkaline, highly fractionated, and strongly peraluminous S-type granites produced by partial melting of metasedimentary rocks (pelite/psammite-derived melts).

To identify the tectonic settings of granitic magmatism and provide a geodynamic explanation for the generation of S-type granitoids in the present study, we used several tectonic discrimination diagrams. We compiled available data on Early Cretaceous igneous rocks of active continental margins from Li et al. (2016), Aminov et al. (2017) and Liu et al. (2020b) from the Southern Pamir, and Early Cretaceous S-type granite data from the Rushan-Pshart zone, which we plotted in combination with our data (Figure 11). The continental arc rocks were distinctive from the S-type granites and plots in the volcanic arc and syn-to post-collisional fields (Figure 11). We aimed to define whether the granites from this study belonged to volcanic arc, within-plate, oceanic ridge, or collisional granites by utilizing the Ta vs. Yb diagram, the results of which clearly showed that the granites were collisional-related (Figure 11A). In the triangle tectonic discrimination diagram (Hf vs. Ta*3 vs. Rb/13) of Harris et al. (1986), the samples plotted within the syn to post-collisional fields (Figure 11C). However, in the Rb vs. Y+Nb plot by Pearce (1996) and Rb vs. Yb+Ta diagrams, the samples fell within the post-collisional fields (Figures 11A,C).
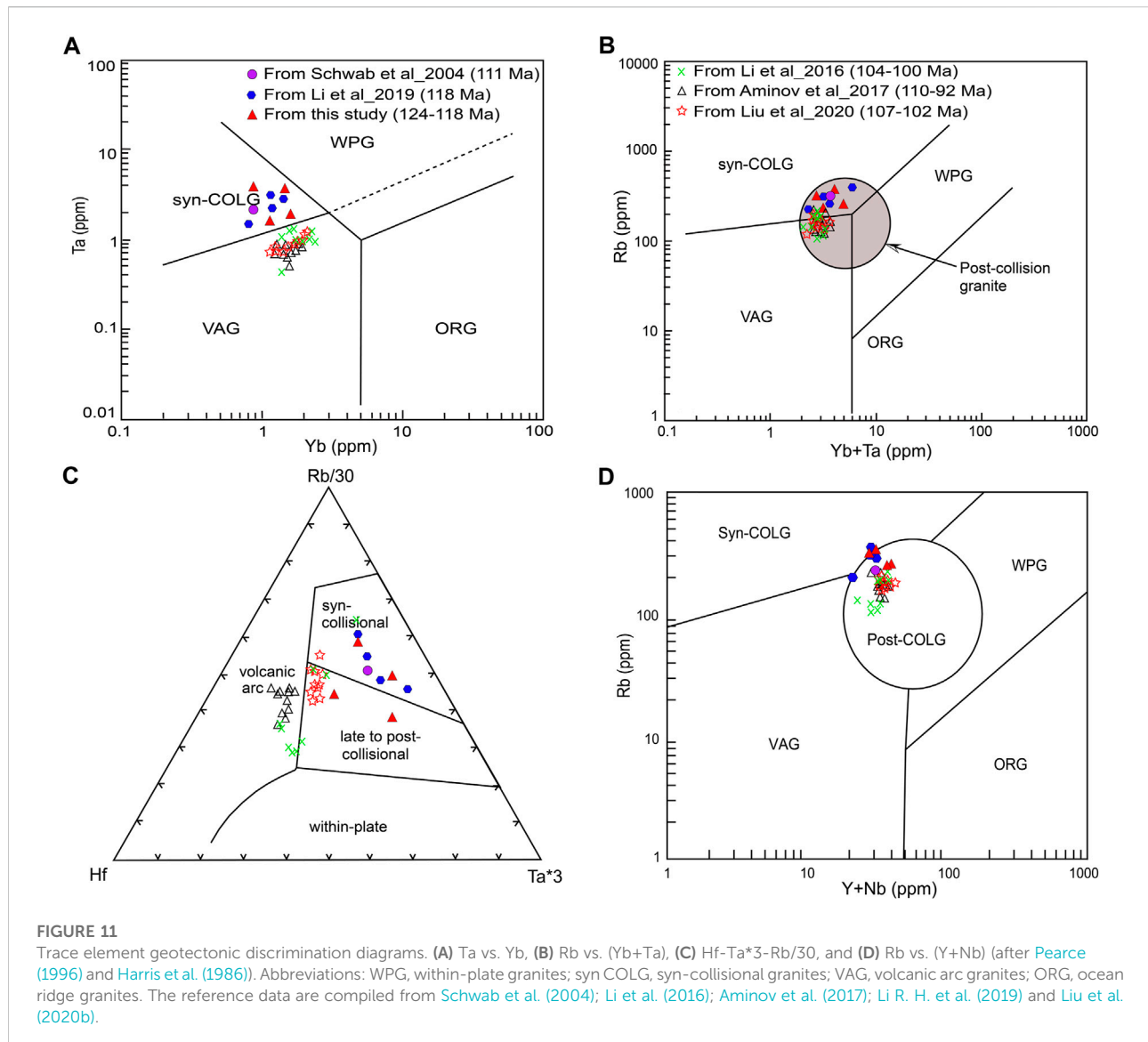
The sample from Schwab et al. (2004) (111 Ma; S-type granite) similarly fell in syn-collisional to the post-collisional fields (Figures 11B–D). The samples from Li R. H. et al. (2019) (118 Ma) fell into the syn to post-collisional or syn-collisional

fields (Figures 11A–D). S-type granites can form in both syn and post-collisional settings (Barbarin, 1996). However, the early Cretaceous granites are highly fractionated S-type granites, which suggests that they formed in an extensional environment. This is inconsistent with the tectonic setting discrimination diagram, which shows a post-collisional setting. Furthermore, the granites had high zircon saturation temperatures (T_{Zr} = 746–813), except for sample Psh-1, which showed a lower temperature (T_{Zr} = 682), consistent with characteristics of post-collisional granites (Liu X. et al., 2021). S-type granites contain abundant inherited zircons; however, our samples showed little inheritance of zircons. This suggests that the samples were dry granites that may have been produced through dehydration (heat fluxed) melting at high temperatures, thus containing small amounts of zircons, compared to wet granites (hydrate melting) that form at lower temperatures and contain abundant inherited zircons (Bea et al., 2021). This implies that the granites were produced in high-temperature dehydration melting conditions with a thermal supply underneath.

Sample Psh-1 had a lower zircon saturation temperature (T_{Zr} = 682); however, Clemens et al. (2020) suggested that lower zircon saturation temperatures do not necessarily indicate that the granitic melt was generated in a low-temperature environment. Clemens et al. (2020) and Zheng and Gao (2021) concluded that most crustal-derived melt (S-type granite) was produced in high-temperature conditions through dehydration (fluid absent) melting in an extensional environment. The mafic magma underplating serves as a driven force/or heat source that causes melting of the supracrustal metasedimentary rocks (Sylvester, 1998; Gao et al., 2016b; Clemens et al., 2020). Therefore, we attributed this concept to our studied granites, which were formed and emplaced in the same way, as shown in the petrogenesis and discrimination diagrams. We concluded that the granitic rocks in the present study formed in an initial post-collisional setting in an extensional environment. Our conclusion is consistent with those reported highly fractionated S-type granites, which were interpreted to form in an extensional environment (Huang and Jiang, 2014; Zhu et al., 2020; Liu X. et al., 2021).

5.2.2 Mafic dikes

We did not obtain a precise age (only a single-zircon age of 121 Ma; Figure 4E) to constrain the exact emplacement time of the diabase dikes (samples of Psh-6; 7). The dikes intruded the Early Cretaceous granitic pluton of 124–118 Ma, suggesting a younger age than 124 Ma (Figures 3A,B). Thus, we tentatively interpreted them to have formed in the late Early Cretaceous, nearly contemporaneous with granitic rocks from this study. Hydrothermal alteration and post-emplacement metamorphism can change/or modify the concentration of mobile elements such as Na, K, R, B, Sr, and Pb (Hart and Staudigel, 1982; Photiades et al., 2003). It is generally accepted that the high-field strength

FIGURE 11
Trace element geotectonic discrimination diagrams. **(A)** Ta vs. Yb, **(B)** Rb vs. (Yb+Ta), **(C)** Hf-Ta*3-Rb/30, and **(D)** Rb vs. (Y+Nb) (after Pearce (1996) and Harris et al. (1986)). Abbreviations: WPG, within-plate granites; syn COLG, syn-collisional granites; VAG, volcanic arc granites; ORG, ocean ridge granites. The reference data are compiled from Schwab et al. (2004); Li et al. (2016); Aminov et al. (2017); Li R. H. et al. (2019) and Liu et al. (2020b).
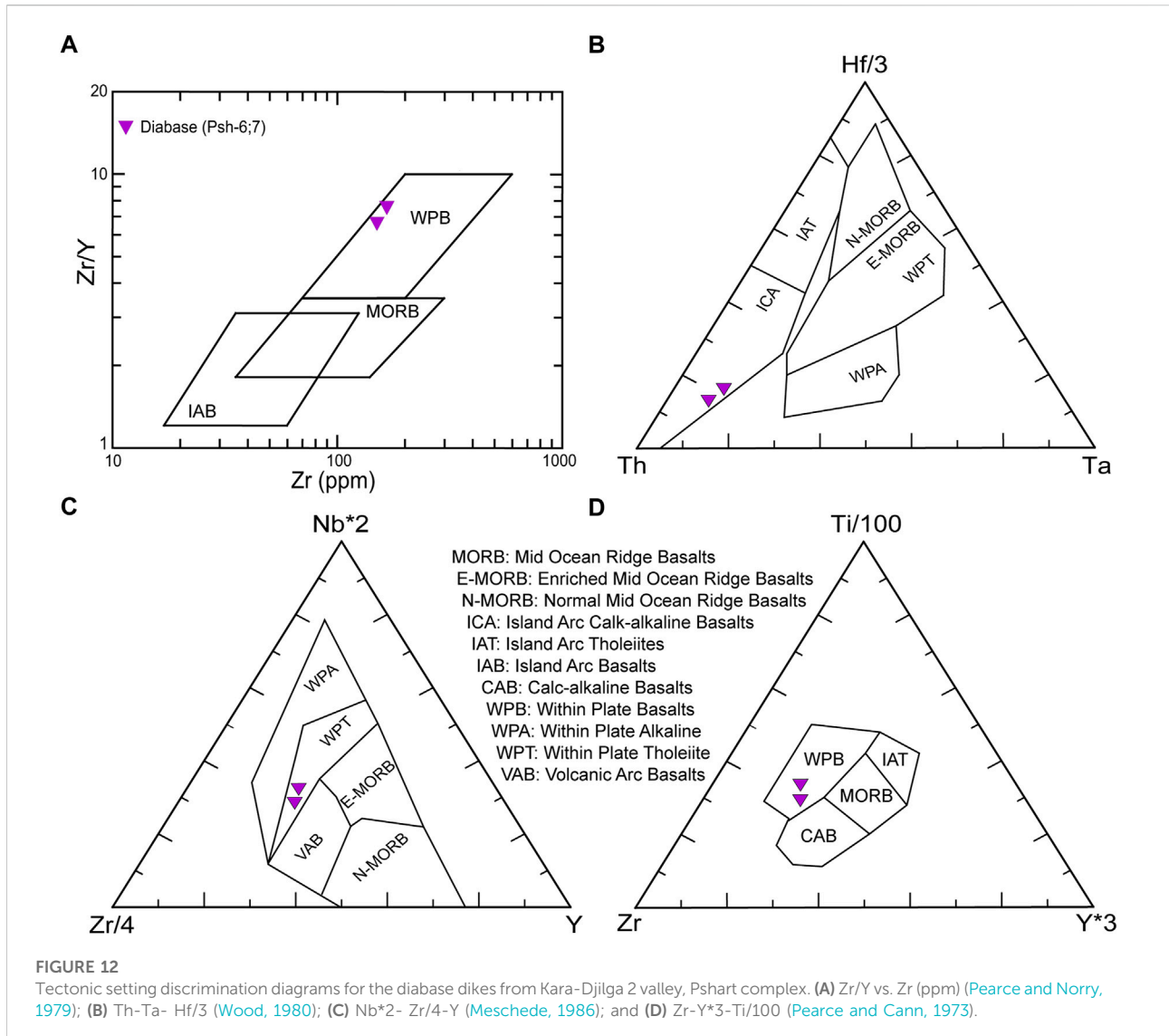
elements (HFSEs) are less susceptible to alteration (Floyd and Winchester, 1975). Therefore, we used HFSEs (Zr, Y, Nb, Th, Ta, and Hf) to decipher the tectonic setting of the mafic dikes.

The samples showed alkaline affinity (Figure 5A; Supplementary Table S2B) but plotted within the field of within-plate tholeiite rocks on Th-Ta-Hf/3 (Figure 12B). In the Zr vs. Zr/Y and Zr-Y*3-Ti/100 diagrams, the samples plotted in the within-plate basalt field (Figures 12A,D). Thus, the geochemical data favor that the diabase dikes that intruded the Early Cretaceous granites formed in an extensional tectonic setting immediately after the Early Cretaceous granites. However, the samples plotted within the field of the island arc calk-alkaline basalt in the Th-Ta-Hf/3 diagram, suggesting that the mantle sources were metasomatized (giving an arc-related signature to the diabase dikes) by slab-released components, which is

consistent with the Th/Nb and U/Th diagrams (Figure 10). Therefore, the mafic diabase dikes were derived from a metasomatized mantle source in an extensional environment.

5.3 Closure timing and post-collisional magmatism

The Central and Southern Pamir (Cimmerides) are the detached fragments/blocks of Gondwana, which drifted northward during the opening of the Neo-Tethys Ocean and amalgamated to the southern margin of Eurasia in the Mesozoic (Sengör, 1979; Burtman and Molnar, 1993; Schwab et al., 2004; Burtman, 2010; Robinson et al., 2012; Angiolini et al., 2013, 2015; Villarreal et al., 2020). Nowadays, the RPSZ marks the site where

FIGURE 12
Tectonic setting discrimination diagrams for the diabase dikes from Kara-Djilga 2 valley, Pshart complex. **(A)** Zr/Y vs. Zr (ppm) (Pearce and Norry, 1979); **(B)** Th-Ta- Hf/3 (Wood, 1980); **(C)** Nb*2- Zr/4-Y (Meschede, 1986); and **(D)** Zr-Y*3-Ti/100 (Pearce and Cann, 1973).

the Central and Southern Pamir terranes collided after the complete consumption of the Rushan–Pshart Ocean. Generally, the rifting time between the Central and Southern Pamir has been interpreted as the Early Permian to Middle Triassic, based on the Lower Permian basaltic rocks within the western Pshart zone and SE Pamir (Shindy Formation) (Pashkov and Shvol′man, 1979; Leven, 1995; Angiolini et al., 2015). However, it remains unclear whether the Rushan–Pshart Ocean was completely consumed by the Late Triassic–Early Jurassic or later. Several studies suggested the Late Triassic–Early Jurassic coalescence of the Central and Southern Pamir based on the Cimmerian nonconformity in the Southern Pamir (Angiolini et al., 2013; Robinson, 2015; Chapman et al., 2018a; Villarreal et al., 2020). The presence of Late Triassic I-type arc-related granitoids (206-201Ma; U-Pb

dating) on the southern edge of the Central Pamir led Wang S. et al. (2020) to the same conclusion.

However, several lines of evidence contradict these interpretations:

1) The presence of 198–170 Ma arc-related granitic intrusions in the southernmost part of the Pshart complex (Schwab et al., 2004; Chapman et al., 2018b) and the Late Jurassic cooling age (Schwab et al., 2004). Schwab et al. (2004) also reported the 151 Ma ($^{40}Ar/^{39}Ar$ of muscovite) monzogranite pebble (sample 96P4e) from the conglomerate of possibly Miocene ages within the western Pshart intermontane valley.
2) The presence of andesite, andesitic basalt, and tuff in combination with limestone and sandstone and deep marine rocks, including chert and cherty-shale, of Late

Jurassic age (Etchki–Tushar Formation) (Pashkov and Shvol'man, 1979; Leven, 1995), suggests magmatic activity and presence of the oceanic basin by that time.

3) The presence of a 118-Ma two-mica monzogranite with strongly peraluminous S-type granite characteristics in the south-western part of the Central Pamir has been interpreted to form in a syn-collisional setting during the final closure of the Rushan–Pshart Ocean (Li R. H. et al., 2019). A slightly younger two-mica monzogranite of 111 Ma (Rb-Sr age; sample P7) from the Pshart complex was interpreted as being syn-collisional (Schwab et al., 2004) (Figure 1).

4) The presence of strongly deformed carbonate rocks of the Central and Southern Pamir, with a non-conforming overlay of sandstones and conglomerates of Cretaceous age, reported by Shvol'man (1978) and Ruzhentsev and Shvol'man (1981), was associated with the closure timing of the Rushan–Pshart Ocean.

Therefore, the closure timing of the Rushan–Pshart Ocean may have been younger than the Late Triassic–Early Jurassic. The volcaniclastic sandstone in the southernmost Central Pamir (111 Ma) bears a strong similarity to the Cretaceous sedimentary and volcanic rocks of the Bangong–Nujiang zone and northern Lhasa terrane (He et al., 2019). We agree with He et al. (2019) that the proposed Cimmerian nonconformity (Permian–Triassic strata composed of quartzite, slate, and carbonate) possibly formed in retro-arc deformation during the subduction of the Rushan–Pshart oceanic lithosphere rather than the collision of the Central and Southern Pamir.

Our petrological, geochemical, and geochronological data revealed that the 124–118 Ma granites were highly fractionated, strongly peraluminous S-type granite generated from the partial melting of metasedimentary rocks in an initial post-collisional stage (Figure 13A). These findings were deduced from mostly well-studied regions such as the Himalayas, Alps, and other orogens in which the post-collisional granites were emplaced after 5–20 Ma (maximum 26 Ma), following the main collisional events (Sylvester, 1998; Zheng and Gao, 2021). If the Late Triassic to Early Jurassic collision of the Central and Southern Pamir were the case (Villarreal et al., 2020), it would take ca. 75 Ma for the emplacement of post-collisional granitoids in this study, which is unlikely. This is also not consistent with the four facts and/or arguments aforementioned. Therefore, it is likely that the granites were emplaced immediately after the final closure of the Rushan–Pshart Ocean in the Late Jurassic–Early Cretaceous. This view is supported by the presence of the volcanic rocks and cherts of the Late Jurassic and the absence of younger ages (as described in the previous section). The minimum U-Pb age for the inherited zircon from the granites is the late Lower Jurassic (180 Ma; Figure 4C), indicating active sedimentation by that time. The Late Jurassic to Early Cretaceous compressional tectonic switched to an extensional regime, as indicated by the post-collisional, highly fractionated peraluminous S-type

granites. The mafic dikes were emplaced in an extensional setting (Figures 12A,C,D). In the Th-Ta-Hf/3 diagram, the samples plot in the island arc calk-alkaline basalt field (Figure 12B), implying that the slab-released fluids of the foundered Rushan–Pshart oceanic lithosphere compositionally modified the upwelling asthenospheric mantle (Figure 10).

After the Late Jurassic–Early Cretaceous closure and collision of the Central and Southern Pamir, the oceanic lithosphere sank after detachment, which caused an upwelling of mafic magma and its underplating, which constituted the heat source for the partial melting of metasedimentary rocks. Furthermore, the partially melted and segregated granitic magma underwent fractional crystallization during its ascent and emplacement. Continuous local extension, asthenospheric mantle upwelling, and lithospheric thinning caused the emplacement of the diabase dikes (Figure 13C).

5.4 Implications for the suture/terrane correlations associated with the closure of Meso-Tethys Ocean

The Cenozoic India–Asia collision and the northward translation of Pamir relative to the Tibetan Plateau make the current terranes and suture correlations very complicated (Figure 1) (Burtman and Molnar, 1993; Sobel and Dumitru, 1997; Lacassin et al., 2004; Robinson, 2009; Cowgill, 2010). It is not clear whether the Rushan–Pshart Ocean is the Meso-Tethys or Paleo-Tethys Ocean. One group of scholars correlated the RPSZ to the Longmu Co-Shuanghu suture zone (Burtman and Samygin, 2001; Burtman, 2010; Angiolini et al., 2013; Wang S. et al., 2020; Liu et al., 2020c), which bisects the Northern and Southern Qiantang terranes (Liu et al., 2011; Liang et al., 2012; Zhao et al., 2015). Another group of scholars directly connected the RPSZ to the Bangong–Nujiang suture (Lacassin et al., 2004; Schwab et al., 2004; Valli et al., 2008; Li R. H. et al., 2019), thus considering it to preserve the remnant of the Meso-Tethys Ocean (Shvol'man, 1978; Burtman and Molnar, 1993; Burtman, 1994). To the west in Afghanistan, the Farah-Rud zone likely represents the extension of the RPSZ (Tapponnier et al., 1981; Montenat, 2009). Zanchetta et al. (2018) considered the RPSZ to be an independent suture that was not correlated to any of the aforementioned sutures.

Several lines of similarities and arguments between the RPSZ-Southern Pamir and Bangong–Nujiang and Lhasa terrane are discussed below.

The deformation and thrusting of Cretaceous strata in the Southern Pamir and Central Pamir (Chapman et al., 2018a; He et al., 2019) resemble those of the Cretaceous non-marine strata (southward propagation) of the Bangong–Nujiang suture and northern Lhasa terrane (Kapp et al., 2007; Volkmer et al., 2014; Sun et al., 2015).

Regarding the evolution and subduction polarity of the Bangong–Nujiang Ocean, a northward (Yin and Harrison,
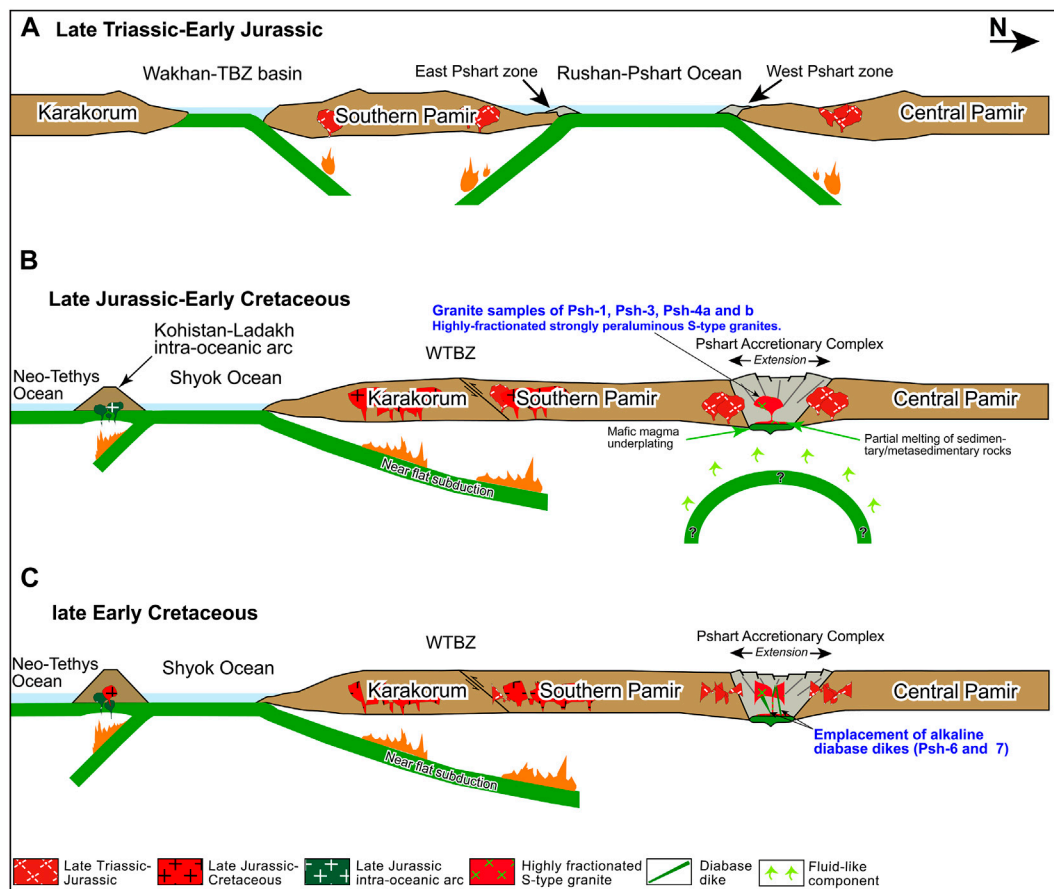
FIGURE 13
Schematic illustration of the Mesozoic evolution of Pamir: **(A)** Initiation of double-sided subduction of the Rushan−Pshart oceanic lithosphere, initial growth of accretionary complexes (East and West Pshart zones), and generation of the Late Triassic−Early Jurassic arc granitoids in the Central and Southern Pamir; **(B)** Late Jurassic−Early Cretaceous collision of the Central and Southern Pamir, underplating of the mafic magma and partial melting of the sedimentary/metasedimentary rocks, and emplacement of highly fractionated, strongly peraluminous S-type granite in the initial post-collisional setting. **(C)** Subsequent extension and emplacement of diabase dikes. The northward subduction is adapted from Wang S. et al. (2020). The southward subduction of the Shyok oceanic lithosphere and formation of the Kohistan−Ladakh intra-oceanic arc were adapted from Saktura et al. (2021).

2000; Li et al., 2014; Liu et al., 2017), southward (Zhu et al., 2013; Li S M et al., 2018; Ma et al., 2020), or double-sided subduction and subsequent "soft collision" have been proposed (Fan et al., 2014a; 2014b; Wang et al., 2016; Zhu et al., 2016; Tang et al., 2018; Li S. et al., 2019; Liu H. et al., 2020). For the Rushan–Pshart Ocean, the southward (Angiolini et al., 2013; Robinson, 2015; Zanchetta et al., 2018; Yogibekov et al., 2020), northward (Schwab et al., 2004; Wang S. et al., 2020), and possibly double-sided subduction (Robinson et al., 2012; Robinson, 2015; Li R. H. et al., 2019) have been proposed. The Upper Triassic–Jurassic plutons are pervasively intruded to either side of the RPSZ (Figures 1, 2A), which were formed during the double-sided subduction. The Eastern and Western Pshart zones developed in different subduction zones (Leven, 1995; Zanchetta et al., 2018). The lithology of the Eastern Pshart zone greatly differs from that of the Western Pshart zone, with only basalts

common between zones. However, the basaltic rocks from the West Pshart are Early Permian, while those of the East Pshart are Late Permian to Triassic (Pashkov and Shvol′man, 1979; Leven, 1995). In this context, we depict the double-sided subduction for the Rushan–Pshart Ocean (Figure 13A). No high-grade metamorphic rocks have been documented along the RPSZ and the Bangong–Nujiang suture likely does not preserve Cretaceous high-grade metamorphic rocks, which reflects a soft collision (arc–arc collision) (Zhu et al., 2016). Conversely, the Longmu Cu-Shuanghu suture is defined by an exposed high-pressure metamorphic belt from the Triassic. The Longmu Co-Shuanghu Paleo-Tethys Ocean opened in the Early Ordovician to Silurian (480–428 Ma) and closed by the Middle Triassic (220 Ma) (Zhai et al., 2013b, 2016, 2011; Hu et al., 2014; Metcalfe, 2021). The newly discovered Silurian subduction-related rocks in the northern margin of the South Qiangtang

terrane (Xiangtaohu intrusive complex; 430–437 Ma) are evidence for the southward subduction of the Proto-Tethys Longmu Co-Shuanghu Ocean by that time (Liu H. et al., 2021). In contrast, the opening time of the Rushan–Pshart Ocean has been interpreted as the Late Carboniferous–Early Permian to the Middle Triassic (Pashkov and Shvol'man, 1979; Burtman and Molnar, 1993; Leven, 1995; Angiolini et al., 2015). Similarly, the opening time of the Bangong–Nujiang Meso-Tethys Ocean is considered to be the Late Carboniferous–Early Permian (Pan et al., 2006; Zhai et al., 2013a; Chen S. S. et al., 2017; Fan et al., 2021c), with a close timing of the Late Jurassic–Early Cretaceous (Li S. et al., 2020; Li et al., 2019 S.; Hu et al., 2019; Wang W. et al., 2020; Ma et al., 2020; Fan et al., 2021b). In this study, we concluded that the Rushan–Pshart Ocean closed in the Late Jurassic–Early Cretaceous (section 5.3; Figure 13B). The Late Carboniferous–Early Permian opening of the Rushan–Pshart and Bangong–Nujiang Oceans was associated with mantle plume activity (Pashkov and Shvol'man, 1979; Leven, 1995; Angiolini et al., 2013; Fan et al., 2021c). However, the formation of the Longmu-Co Shuanghu Ocean was induced with a back-arc basin opening in response to the southward subduction of the Proto-Tethys oceanic lithosphere (Xu et al., 2020; Metcalfe, 2021).

The Early Cretaceous arc-related igneous rocks are widespread in the Southern Pamir (105 Ma high flux event) and represent the product of a northward subduction of the Neo-Tethyan (Shyok) oceanic lithosphere (Schwab et al., 2004; Aminov et al., 2017; Chapman et al., 2018b; Liu et al., 2020b). In the Tibetan Plateau, Cretaceous magmatism with high a flux event occurring 110 Ma is widely distributed in the Lhasa terrane, which is interpreted to have formed in response to the near-flat northward subduction of the Neo-Tethys oceanic lithosphere (Zhang et al., 2010; Zhang K.-J. et al., 2012; Kang et al., 2014; Zheng et al., 2019), southward subduction of the Bangong-Nujiang Ocean, or a combination of both (Du et al., 2011; Zhu et al., 2013; Li Y et al., 2018; Ma et al., 2020). Jurassic arc-related granitoids of 198–170 Ma have been reported from the southern edge of the Pshart complex (Schwab et al., 2004; Chapman et al., 2018b), which are identical to the arc-related granitoids (185–170 Ma) of the Amdo region (Guynn et al., 2006). A systematic study of sedimentary rocks in the Garze area of the Bangong–Nujiang suture revealed that the sediments were sourced from the Early Jurassic arc of the Southern Qiantang terrane, which may have been completely eroded (Li S. et al., 2019). These findings fit well and record a similar pre-Cenozoic history of the Southern Pamir–RPSZ and Bangong–Nujiang suture and Lhasa terrane and differ greatly from that of the Longmu Co-Shuanghu zone.

However, the relative movement along the Karakoram fault hampered the correlations of the RPSZ and Bangong–Nujiang suture, which requires a displacement of up to 300 km. Seismological and receiver functions studies revealed 300 km

of subducted Asian crust beneath Pamir, thus assuming the same amount for the northward translation of Pamir relative to the major part of the Tibetan Plateau (Burtman and Molnar, 1993; Schneider et al., 2019; Bloch et al., 2021; Xu et al., 2021). Robinson (2009) reported a displacement of approximately 167 km along the Karakoram fault based on the results of the analysis of satellite images of the Upper Triassic–Lower Jurassic carbonates of the Aghil Formation. A recent study in the northeastern Pamir proposed that the present curvature shape of the Pamir orogen is inherited from Late Paleozoic embayment with negligible left-lateral displacement along the Darvaz fault, rather than due to a Cenozoic northward translation (Li Y.-P. et al., 2020). All these facts support the complicated geological structure of the Pamir, thus making it difficult to precisely define the amount of its displacement relative to the adjacent regions. Additional undocumented displacements may also exist along the Karakoram fault and its branches. More broadly, it is noteworthy that the RPSZ–Bangong-Nujiang and Southern Pamir-Lhasa terrane have similar pre-Cenozoic tectono-magmatic histories (as aforementioned), as well as the opening and closure timings of the oceans.

Thus, based on our observations and the aforementioned discussion, we tentatively propose that the Bangong–Nujiang zone may represent the eastern extension of the RPSZ and that the Farah–Rud zone is the possible western "time-correlative"/continuation of the given suture. However, we cannot preclude the possibility that the Rushan–Pshart Ocean evolved separately without a direct connection to the east, as proposed by Zanchetta et al. (2018). We consider the Rushan–Pshart Ocean to be the Meso-Tethys Ocean.

6 Conclusion

The data on granites and diabase dikes newly acquired in the present study, combined with previously published data, suggest the following conclusions.

1) The Early Cretaceous granites from the Pshart complex were emplaced during 124–118 Ma and are interpreted here as highly fractionated, strongly peraluminous S-type granite.
2) The underplating of mafic magma served as a heat source for the partial melting of metasedimentary rocks. The granitic melt formed in a plagioclase stability field and underwent subsequent fractional crystallization during its ascent.
3) The diabase dikes were derived from a metasomatized source and were emplaced within an extensional tectonic setting.
4) The Early Cretaceous, highly fractionated, and strongly peraluminous S-type granites of the Pshart complex represent the product of metasedimentary-derived melt, which were formed in the post-collisional environment after the final closure of the Rushan–Pshart Meso-Tethys Ocean. Thus, the studied rocks record the change in

geodynamic regime from compressional to extensional. The diabase dikes were emplaced during subsequent continued local extension.

5) The RPSZ may represent the western continuation of the Bangong–Nujiang suture of the Tibetan Plateau and it is "time-correlative" to the Farah-Rud zone in Afghanistan.

Data availability statement

The original contributions presented in the study are included in the article/Supplementary Material; further inquiries can be directed to the corresponding authors.

Author contributions

DY and MS wrote the article. WX, YM, CZ, HY, and QM revised the manuscript, conceived the experiments, and contributed to the data interpretation. The fieldwork and preliminary study of samples were carried out by JA, GK, and SA. HY conducted the geochemical analyses. All authors have read and agreed to the published version of the manuscript.

Funding

Acknowledgments

Conflict of interest

The authors declare that the research was conducted in the absence of any commercial or financial relationships that could be construed as a potential conflict of interest.

Publisher's note

All claims expressed in this article are solely those of the authors and do not necessarily represent those of their affiliated organizations, or those of the publisher, the editors, and the reviewers. Any product that may be evaluated in this article, or claim that may be made by its manufacturer, is not guaranteed or endorsed by the publisher.

Supplementary material

The Supplementary Material for this article can be found online at: https://www.frontiersin.org/articles/10.3389/feart.2022.1090952/full#supplementary-material

References

Aminov, J., Ding, L., Mamadjonov, Y., Dupont-Nivet, G., Aminov, J., Zhang, L.-Y., et al. (2017). Pamir Plateau formation and crustal thickening before the India-Asia collision inferred from dating and petrology of the 110–92 Ma Southern Pamir volcanic sequence. *Gondwana Res.* 51, 310–326. doi:10.1016/j.gr.2017.08.003

Angiolini, L., Zanchi, A., Zanchetta, S., Nicora, A., and Vezzoli, G. (2013). The cimmerian geopuzzle: New data from South Pamir. *Terra* 25, 352–360. doi:10.1111/ter.12042

Angiolini, L., Zanchi, A., Zanchetta, S., Nicora, A., Vuolo, I., Berra, F., et al. (2015). From rift to drift in South Pamir (Tajikistan): Permian evolution of a Cimmerian terrane. *J. Asian Earth Sci.* 102, 146–169. doi:10.1016/j.jseaes.2014.08.001

Barbarin, B. (1999). A review of the relationships between granitoid types, their origins and their geodynamic environments. *Lithos* 46, 605–626. doi:10.1016/s0024-4937(98)00085-1

Barbarin, B. (1996). Genesis of the two main types of peraluminous granitoids. *Geol.* 24, 295–298. doi:10.1130/0091-7613(1996)024<0295:gottmt>2.3.co;2

Bartoli, O., Cesare, B., Poli, S., Bodnar, R. J., Acosta-Vigil, A., Frezzotti, M. L., et al. (2013). Recovering the composition of melt and the fluid regime at the onset of crustal anatexis and S-type granite formation. *Geology* 41, 115–118. doi:10.1130/G33455.1

Bea, F., Morales, I., Molina, J. F., Montero, P., and Cambeses, A. (2021). Zircon stability grids in crustal partial melts: Implications for zircon inheritance. *Contrib. Mineral.* . 176, 18–13. doi:10.1007/s00410-021-01772-x

Beard, J. S., Abitz, R. J., and Lofgren, G. E. (1993). Experimental melting of crustal xenoliths from Kilbourne Hole, New Mexico and implications for contamination and Genesis of magmas. *Contr. Mineral.* . 115, 88–102. doi:10.1007/BF00712981

Bloch, W., Schurr, B., Yuan, X., Ratschbacher, L., Reuter, S., Kufner, S. K., et al. (2021). Structure and stress field of the lithosphere between Pamir and tarim. *Geophys. Res. Lett.* doi:10.31223/X5N60C

Burtman, V., and Samygin, S. (2001). Tectonic evolution of high Asia in the paleozoic and mesozoic. *Geotectonics* 35, 276–294.

Burtman, V. S. (1994). Meso-Tethyan oceanic sutures and their deformation. *Tectonophysics* 234, 305–327. doi:10.1016/0040-1951(94)90230-5

Burtman, V. S., and Molnar, P. H. (1993). Geological and geophysical evidence for deep subduction of continental crust beneath the Pamir. *Geol. Soc. Am. Special Pap.* 281, 1–76. doi:10.1130/SPE281-p1

Burtman, V. S. (2010). Tien Shan, Pamir, and Tibet: History and geodynamics of phanerozoic oceanic basins. *Geotecton.* 44, 388–404. doi:10.1134/S001685211005002X

Champion, D. C., and Bultitude, R. J. (2013). The geochemical and Sr-Nd isotopic characteristics of Paleozoic fractionated S-types granites of north Queensland: Implications for S-type granite petrogenesis. *Lithos* 162, 37–56. doi:10.1016/j.lithos.2012.11.022

Chapman, J. B., Robinson, A. C., Carrapa, B., Villarreal, D., Worthington, J., DeCelles, P. G., et al. (2018a). Cretaceous shortening and exhumation history of the South Pamir terrane. *Lithosphere* 10, 494–511. doi:10.1130/L691.1

Chapman, J. B., Scoggin, S. H., Kapp, P., Carrapa, B., Ducea, M. N., Worthington, J., et al. (2018b). Mesozoic to cenozoic magmatic history of the Pamir. *Earth Planet. Sci. Lett.* 482, 181–192. doi:10.1016/j.epsl.2017.10.041

Chappell, B. (1999). Aluminium saturation in I-and S-type granites and the characterization of fractionated haplogranites. *Lithos* 46, 535–551. doi:10.1016/S0024-4937(98)00086-3

Chappell, B., and White, A. (1992). I-And S-type granites in the lachlan fold belt. *Trans. R. Soc. Edinb. Earth Sci.* 83, 1–26. doi:10.1130/SPE272-p1

Chappell, B., and White, A. (1974). Two contrasting granite types. Pacif. *Geology* 8, 173–174.

Chappell, B. W., and White, A. J. (2001). Two contrasting granite types: 25 years later. *Aust. J. earth Sci.* 48, 489–499. doi:10.1046/j.1440-0952.2001.00882.x

Chen, S., Chen, H., Zhu, K., and Tao, Y. (2021). Petrogenesis of the middle–late triassic S-and I-type granitoids in the eastern Pamir and implications for the tanymas–jinshajiang Paleo-Tethys Ocean. *Int. J. Earth Sci.* 110, 1213–1232. doi:10.1007/s00531-021-02013-z

Chen, S. S., Shi, R. D., Fan, W. M., Gong, X. H., and Wu, K. (2017a). Early Permian mafic dikes in the Nagqu area, central Tibet, China, associated with embryonic oceanic crust of the Meso-Tethys Ocean. *J. Geophys. Res. Solid Earth* 122, 4172–4190. doi:10.1002/2016JB013693

Chen, Y.-X., Zhou, K., and Gao, X.-Y. (2017b). Partial melting of ultrahigh-pressure metamorphic rocks during continental collision: Evidence, time, mechanism, and effect. *J. Asian Earth Sci.* 145, 177–191. doi:10.1016/j.jseaes.2017.03.020

Clarke, D. B. (2019). The origins of strongly peraluminous granitoid rocks. *Can. Mineralogist* 57, 529–550. doi:10.3749/canmin.1800075

Clemens, J. D., Stevens, G., and Bryan, S. E. (2020). Conditions during the formation of granitic magmas by crustal melting–hot or cold; drenched, damp or dry? *Earth-Science Rev.* 200, 102982. doi:10.1016/j.earscirev.2019.102982

Clemens, J. (2003). S-Type granitic magmas—Petrogenetic issues, models and evidence. *Earth-Science Rev.* 61, 1–18. doi:10.1016/S0012-8252(02)00107-1

Clemens, J., and Stevens, G. (2012). What controls chemical variation in granitic magmas? *Lithos* 134, 317–329. doi:10.1016/j.lithos.2012.01.001

Corfu, F., Hanchar, J. M., Hoskin, P. W., and Kinny, P. (2003). Atlas of zircon textures. *Rev. Mineral. Geochem.* 53, 469–500. doi:10.2113/0530469

Cowgill, E. (2010). Cenozoic right-slip faulting along the eastern margin of the Pamir salient, northwestern China. *Geol. Soc. Am. Bull.* 122, 145–161. doi:10.1130/B26520.1

Dong, Y., Zhang, G., Neubauer, F., Liu, X., Hauzenberger, C., Zhou, D., et al. (2011). Syn-and post-collisional granitoids in the central tianshan orogen: Geochemistry, geochronology and implications for tectonic evolution. *Gondwana Res.* 20, 568–581. doi:10.1016/j.gr.2011.01.013

Donnely, K. E., Goldstain, S. L., Langmuir, C. H., and Spiegelman, M. (2004). Origin of enriched ocean ridge basalts and implications for mantle dynamics. *Earth Planet. Sci. Lett.* 226, 347–366. doi:10.1016/j.epsl.2004.07.019

Dronov, V. I. (1964). On the south boundary of Central Pamir. Dushanbe (in Russia). *Mater. po Geol. Pamira* 2, 133–137.

Du, D., Qu, X., Wang, G., Xin, H., and Liu, Z. (2011). Bidirectional subduction of the middle tethys oceanic basin in the west segment of bangonghu-nujiang suture, Tibet: Evidence from zircon U-Pb LAICPMS dating and petrogeochemistry of arc granites. *Acta Petrol. Sin.* 27, 1993–2002.

Fan, B., Liu, M., He, Z., Meng, G., Ma, Z., and Li, L. (2021a). Mesozoic-cenozoic tectonic evolution and uplift in Pamir: Application of fission track thermochronology. *Acta Geol. sinica-. Engl. Ed.* 95, 780–793. doi:10.1111/1755-6724.14671

Fan, J.-J., Li, C., Xie, C.-M., and Wang, M. (2014a). Petrology, geochemistry, and geochronology of the zhonggang ocean island, northern Tibet: Implications for the evolution of the banggongco–nujiang oceanic arm of the neo-tethys. *Int. Geol. Rev.* 56, 1504–1520. doi:10.1080/00206814.2014.947639

Fan, J.-J., Li, C., Xu, J.-X., and Wang, M. (2014b). Petrology, geochemistry, and geological significance of the Nadong ocean island, Banggongco–Nujiang suture, Tibetan plateau. *Int. Geol. Rev.* 56, 915–928. doi:10.1080/00206814.2014.900651

Fan, J.-J., Niu, Y., Liu, Y.-M., and Hao, Y.-J. (2021b). Timing of closure of the Meso-Tethys Ocean: Constraints from remnants of a 141– 135 Ma ocean island within the Bangong– nujiang suture zone, Tibetan plateau. *GSA Bull.* 133, 1875–1889. doi:10.1130/B35896.1

Fan, J.-J., Niu, Y., Luo, A.-B., Xie, C.-M., Hao, Y.-J., and Liu, H.-Y. (2021c). Timing of the Meso-Tethys Ocean opening: Evidence from permian sedimentary provenance changes in the South Qiangtang terrane, Tibetan plateau. *Palaeogeogr. Palaeoclimatol. Palaeoecol.* 567, 110265. doi:10.1016/j.palaeo.2021.110265

Floyd, P. A., and Winchester, J. (1975). Magma type and tectonic setting discrimination using immobile elements. *Earth Planet. Sci. Lett.* 27, 211–218. doi:10.1016/0012-821X(75)90031-X

Förster, H. J., Tischendorf, G., and Trumbull, R. B. (1997). An evaluation of the Rb vs.(Y+ Nb) discrimination diagram to infer tectonic setting of silicic igneous rocks. *Lithos* 40, 261–293. doi:10.1016/S0024-4937(97)00032-7

Frost, B. R., Barnes, C. G., Collins, W. J., Arculus, R. J., Ellis, D. J., and Frost, C. D. (2001). A geochemical classification for granitic rocks. *J. petrology* 42, 2033–2048. doi:10.1093/petrology/42.11.2033

Gao, L.-E., Zeng, L., and Asimow, P. D. (2017). Contrasting geochemical signatures of fluid-absent versus fluid-fluxed melting of muscovite in metasedimentary sources: The Himalayan leucogranites. *Geology* 45, 39–42. doi:10.1130/G38336.1

Gao, P., Zheng, Y.-F., and Zhao, Z.-F. (2016a). Distinction between S-type and peraluminous I-type granites: Zircon versus whole-rock geochemistry. *Lithos* 258, 77–91. doi:10.1016/j.lithos.2016.04.019

Gao, P., Zheng, Y. F., and Zhao, Z. F. (2016b). Experimental melts from crustal rocks: A lithochemical constraint on granite petrogenesis. *Lithos* 266, 133–157. doi:10.1016/j.lithos.2016.10.005

Girardi, J. D., Patchett, P. J., Ducea, M. N., Gehrels, G. E., Cecil, M. R., Rusmore, M. E., et al. (2012). Elemental and isotopic evidence for granitoid Genesis from deep-seated sources in the Coast Mountains Batholith, British Columbia. *J. petrology* 53, 1505–1536. doi:10.1093/petrology/egs024

Groppo, C., Rolfo, F., McClelland, W. C., and Coble, M. A. (2019). Pre-cenozoic evolution of the Aghil range (Western Tibetan plateau): A missing piece of the tibet-pamir-karakorum geopuzzle. *Gondwana Res.* 69, 122–143. doi:10.1016/j.gr.2018.12.006

Guynn, J. H., Kapp, P., Pullen, A., Heizler, M., Gehrels, G., and Ding, L. (2006). Tibetan basement rocks near Amdo reveal "missing" Mesozoic tectonism along the Bangong suture, central Tibet. *Geol.* 34, 505–508. doi:10.1130/G22453.1

Harris, N. B., Pearce, J. A., and Tindle, A. G. (1986). Geochemical characteristics of collision-zone magmatism. *Geol. Soc. Lond. Spec. Publ.* 19, 67–81. doi:10.1144/gsl.sp.1986.019.01.04

Hart, S. R., and Staudigel, H. (1982). The control of alkalies and uranium in seawater by ocean crust alteration. *Earth Planet. Sci. Lett.* 58, 202–212. doi:10.1016/0012-821X(82)90194-7

He, J., Kapp, P., Chapman, J. B., DeCelles, P. G., and Carrapa, B. J. G. S. (2019). Structural setting and detrital zircon U–Pb geochronology of Triassic–Cenozoic strata in the eastern Central Pamir, Tajikistan. *Geol. Soc. Lond. Spec. Publ.* 483, 605–630. doi:10.1144/SP483.11

Hu, P., Li, C., Wu, Y., Xie, C., Wang, M., and Li, J. (2014). Opening of the Longmu Co–Shuanghu–Lancangjiang ocean: Constraints from plagiogranites. *Chin. Sci. Bull.* 59, 3188–3199. doi:10.1007/s11434-014-0434-z

Hu, W.-L., Wang, Q., Yang, J.-H., Zhang, C., Tang, G.-J., Ma, L., et al. (2019). Late early Cretaceous peraluminous biotite granites along the Bangong–Nujiang suture zone, Central Tibet: Products derived by partial melting of metasedimentary rocks? *Lithos* 344, 147–158. doi:10.1016/j.lithos.2019.06.005

Huang, H.-Q., Li, X.-H., Li, Z.-X., and Li, W.-X. (2015). formation of the jurassic south China large granitic province: Insights from the Genesis of the jiufeng pluton. *Chem. Geol.* 401, 43–58. doi:10.1016/j.chemgeo.2015.02.019

Huang, L.-C., and Jiang, S.-Y. (2014). Highly fractionated S-type granites from the giant dahutang tungsten deposit in jiangnan orogen, Southeast China: Geochronology, petrogenesis and their relationship with W-mineralization. *Lithos* 202, 207–226. doi:10.1016/j.lithos.2014.05.030

Imrecke, D. B., Robinson, A. C., Owen, L. A., Chen, J., Schoenbohm, L. M., Hedrick, K. A., et al. (2019). Mesozoic evolution of the eastern Pamir. *Lithosphere* 11, 560–580. doi:10.1130/l1017.1

Jiang, Z.-Q., Wang, Q., Wyman, D. A., Li, Z.-X., Yang, J.-H., Shi, X.-B., et al. (2014). Transition from oceanic to continental lithosphere subduction in southern Tibet: Evidence from the late cretaceous–early oligocene (~ 91–30 Ma) intrusive rocks in the chanang–zedong area, southern gangdese. *Lithos* 196, 213–231. doi:10.1016/j.lithos.2014.03.001

Kang, Z.-Q., Xu, J.-F., Wilde, S. A., Feng, Z.-H., Chen, J.-L., Wang, B.-D., et al. (2014). Geochronology and geochemistry of the sangri group volcanic rocks, southern Lhasa terrane: Implications for the early subduction history of the neo-tethys and gangdese magmatic arc. *Lithos* 200, 157–168. doi:10.1016/j.lithos.2014.04.019

Kapp, P., DeCelles, P. G., Gehrels, G. E., Heizler, M., and Ding, L. (2007). Geological records of the lhasa-qiangtang and indo-asian collisions in the nima area of central Tibet. *Geol. Soc. Am. Bull.* 119, 917–933. doi:10.1130/B26033.1

Lacassin, R, Valli, F., Arnaud, N., Leloup, P. H., Paquette, J. L., Haibing, L., et al. (2004). Large-scale geometry, offset and kinematic evolution of the Karakorum fault, Tibet. *Earth Planet. Sci. Lett.* 219, 255–269. doi:10.1016/S0012-821X(04)00006-8

Le Bas, M., Le Maitre, R., Streckeisen, A., and Zanettin, B. (1986). A chemical classification of volcanic rocks based on the total alkali-silica diagram. *J. petrology* 27, 745–750. doi:10.1093/petrology/27.3.745

Leven, E. J. (1995). Permian and triassic of the rushan-pshart zone (Pamir). *Riv. Ital. Paleontol. Stratigr.* 101, 3–16.

Li, J., Niu, Y., Hu, Y., Chen, S., Zhang, Y., Duan, M., et al. (2016). Origin of the late early cretaceous granodiorite and associated dioritic dikes in the hongqilafu pluton, northwestern Tibetan plateau: A case for crust–mantle interaction. *Lithos* 260, 300–314. doi:10.1016/j.lithos.2016.05.028

Li, R. H., Peng, B., Zhao, C. S., Yu, M., Song, L. S., and Zhang, H. (2019a). Origin of early creceouscalc-alkaline granite, taxkorgan: Implications for evolution of tethys evolution in central Pamir. *J. Cent. South Univ.* 26, 3470–3487. doi:10.1007/s11771-019-4267-4

Li, S.-M., Zhu, D.-C., Wang, Q., Zhao, Z.-D., Sui, Q.-L., Liu, S.-A., et al. (2014). Northward subduction of bangong–nujiang tethys: Insight from late jurassic intrusive rocks from Bangong tso in Western Tibet. *Lithos* 205, 284–297. doi:10.1016/j.lithos.2014.07.010

Li, S. M., Wang, Q., Zhu, D. C., Stern, R. J., Cawood, P. A., Sui, Q. L., et al. (2018). One or two early Cretaceous arc systems in the Lhasa terrane, southern Tibet. *J. Geophys. Res. Solid Earth* 123, 3391–3413. doi:10.1002/2018JB015582

Li, S., Yin, C., Guilmette, C., and Ding, L. (2020a). Reply to comment by LZ Shi et al. on "Birth and demise of the Bangong–Nujiang Tethyan Ocean: A review from the Gerze area of central Tibet". *Earth-Science Rev.* 208, 103213. doi:10.1016/j.earscirev.2020.103213

Li, S., Yin, C., Guilmette, C., Ding, L., and Zhang, J. (2019b). Birth and demise of the bangong-nujiang tethyan ocean: A review from the gerze area of central Tibet. *Earth-Science Rev.* 198, 102907. doi:10.1016/j.earscirev.2019.102907

Li, Y.-P., Robinson, A. C., Gadoev, M., and Oimuhammadzoda, I. (2020b). Was the Pamir salient built along a Late Paleozoic embayment on the southern Asian margin? *Earth Planet. Sci. Lett.* 550, 116554. doi:10.1016/j.epsl.2020.116554

Li, Y. P., Robinson, A. C., Lapen, T. J., Righter, M., and Stevens, M. K. (2020c). Muztaghata dome Miocene eclogite facies metamorphism: A record of lower crustal evolution of the ne Pamir. *Tectonics* 39, e2019TC005917. doi:10.1029/2019TC005917

Li, Y., Xiao, W., and Tian, Zh. (2018). Early palaeozoic accretionary tectonics of west Kunlun orogen: Insights from datong granitoids, mafic–ultramafic complexes, and silurian–devonian sandstones, Xinjiang, NW China. *Geol. J.* 54, 1505–1517. doi:10.1002/gj.3246

Liang, X., Wang, G., Yuan, G., and Liu, Y. (2012). Structural sequence and geochronology of the qomo ri accretionary complex, central Qiangtang, Tibet: Implications for the late triassic subduction of the Paleo-Tethys Ocean. *Gondwana Res.* 22, 470–481. doi:10.1016/j.gr.2011.11.012

Liu, D., Shi, R., Ding, L., Huang, Q., Zhang, X., Yue, Y., et al. (2017). Zircon U–Pb age and Hf isotopic compositions of mesozoic granitoids in southern Qiangtang, Tibet: Implications for the subduction of the bangong–nujiang tethyan ocean. *Gondwana Res.* 41, 157–172. doi:10.1016/j.gr.2015.04.007

Liu, H., Chen, L., Huang, F., Zeng, Y.-C., and Wang, L.-Q. (2021a). Silurian intermediate–felsic complex in the Xiangtaohu area of central Qiangtang, northern Tibet: Evidence for southward subduction of the Longmuco–Shuanghu Prototethys oceanic plate. *Lithos* 404, 106465–107405. doi:10.1016/j.lithos.2021.106465

Liu, H., Huang, Q., Uysal, I. T., Cai, Z., Wan, Z., Xia, B., et al. (2020a). Geodynamics of the divergent double subduction along the Bangong-Nujiang tethyan suture zone: Insights from late mesozoic intermediate-mafic rocks in central Tibet. *Gondwana Res.* 79, 233–247. doi:10.1016/j.gr.2019.09.018

Liu, X.-Q., Zhang, C.-L., Hao, X.-S., Zou, H., Zhao, H.-X., and Ye, X.-T. (2020b). Early cretaceous granitoids in the southern Pamir: Implications for the meso-tethys evolution of the Pamir Plateau. *Lithos* 362, 105492. doi:10.1016/j.lithos.2020.105492

Liu, X.-Q., Zhang, C.-L., Zou, H., Wang, Q., Hao, X.-S., Zhao, H.-X., et al. (2020c). Triassic-jurassic granitoids and pegmatites from western kunlun-pamir syntax: Implications for the paleo-tethys evolution at the northern margin of the Tibetan plateau. *Lithosphere* 2020, 7282037. doi:10.2113/2020/7282037

Liu, X., Wang, Q., Ma, L., Gou, G.-N., Ou, Q., and Wang, J. (2021b). Late jurassic maofengshan two-mica granites in Guangzhou, south China: Fractional crystallization products of metasedimentary-rock-derived magmas. *Mineral. .* 115, 323–341. doi:10.1007/s00710-020-00733-9

Liu, Y., Santosh, M., Zhao, Z. B., Niu, W. C., and Wang, G. H. (2011). Evidence for palaeo-Tethyan oceanic subduction within central Qiangtang, northern Tibet. *Lithos* 127, 39–53. doi:10.1016/j.lithos.2011.07.023

Ma, X., Song, Y., Tang, J., and Chen, W. (2020). Newly identified rhyolite-biotite monzogranite (A2-type granite)-norite belt from the Bangong-Nujiang collision zone in Tibet Plateau: Evidence for the slab break-off beneath the Lhasa Terrane. *Lithos* 366, 105565. doi:10.1016/j.lithos.2020.105565

Maniar, P. D., and Piccoli, P. M. (1989). Tectonic discrimination of granitoids. *Geol. Soc. Am. Bull.* 101, 635–643. doi:10.1130/0016-7606(1989)101<0635:tdog>2.3.co;2

Meschede, M. (1986). A method of discriminating between different types of mid-ocean ridge basalts and continental tholeiites with the Nb-1bZr-1bY diagram. *Chem. Geol.* 56, 207–218. doi:10.1016/0009-2541(86)90004-5

Metcalfe, I. (2021). Multiple Tethyan ocean basins and orogenic belts in Asia. *Gondwana Res.* 100, 87–130. doi:10.1016/j.gr.2021.01.012

Miller, C. F. (1985). Are strongly peraluminous magmas derived from pelitic sedimentary sources? *J. Geol.* 93, 673–689. doi:10.1086/628995

Montenat, C. (2009). The mesozoic of Afghanistan. *GeoArabia* 14, 147–210. doi:10.2113/geoarabia1401147

Pan, G. T., Mo, X. X., Hou, Z. Q., Zhu, D. C., Wang, L. Q., Li, G. M., et al. (2006). Spatial–temporal framework of the Lhasa orogenic belt and its evolution. *Acta Petrol. Sin.* 22, 521–533.

Pashkov, B. R., and Shvol′man, V. A. (1979). Rift margins of tethys in the pamirs. *Geotectonics* 13, 447–456.

Patiňo Douce, A. E., and Beard, J. S. (1995). Dehydration-melting of biotite gneiss and quartz amphibolite from 3 to 15 kbar. *J. petrology* 36, 707–738. doi:10.1093/petrology/36.3.707

Patiño Douce, A. E., and Harris, N. (1998). Experimental constraints on Himalayan anatexis. *J. petrology* 39, 689–710. doi:10.1093/petroj/39.4.689

Pearce, J. A., and Cann, J. R. (1973). Tectonic setting of basic volcanic rocks determined using trace element analyses. *Earth Planet. Sci. Lett.* 19, 290–300. doi:10.1016/0012-821X(73)90129-5

Pearce, J. A., and Norry, M. J. (1979). Petrogenetic implications of Ti, Zr, Y, and Nb variations in volcanic rocks. *Contr. Mineral. Pet.* 69, 33–47. doi:10.1007/bf00375192

Pearce, J. (1996). Sources and settings of granitic rocks. *Episodes* 19, 120–125. doi:10.18814/epiiugs/1996/v19i4/005

Petro, W. L., Vogel, T. A., and Wilband, J. T. (1979). Major-element chemistry of plutonic rock suites from compressional and extensional plate boundaries. *Chem. Geol.* 26, 217–235. doi:10.1016/0009-2541(79)90047-0

Photiades, A., Saccani, E., and Tassinari, R. (2003). Petrogenesis and tectonic setting of volcanic rocks from the Subpelagonian ophiolitic mélange in the Agoriani area (Othrys, Greece). *Ofioliti* 28, 121–135. doi:10.4454/ofioliti.v28i2.200

Pitcher, W. (1983). *Granite type and tectonic environment,* Symposium on mountain building, 19–40.

Pundir, S., Adlakha, V., Kumar, S., and Singhal, S. (2020). Closure of India–Asia collision margin along the Shyok suture zone in the eastern Karakoram: New geochemical and zircon U–Pb geochronological observations. *Geol. Mag.* 157, 1451–1472. doi:10.1017/S0016756819001547

Qu, J., Zhang, L., Ai, Y., Lü, Z., Wang, J., Zhou, H., et al. (2007). High-pressure granulite from Western Kunlun, northwestern China: Its metamorphic evolution, zircon SHRIMP U-Pb ages and tectonic implication. *Sci. China Ser. D Earth Sci.* 50, 961–971. doi:10.1007/s11430-007-0065-1

Ravikant, V., Wu, F.-Y., and Ji, W.-Q. (2009). Zircon U–Pb and Hf isotopic constraints on petrogenesis of the Cretaceous–Tertiary granites in eastern Karakoram and Ladakh, India. *Lithos* 110, 153–166. doi:10.1016/j.lithos.2008.12.013

Reichardt, H., and Weinberg, R. F. (2012). The dike swarm of the Karakoram shear zone, Ladakh, NW India: Linking granite source to batholith. *Geol. Soc. Am. Bull.* 124, 89–103. doi:10.1130/B30394.1

Rembe, J., Sobel, E. R., Kley, J., Zhou, R., Thiede, R., and Chen, J. (2021). The carboniferous arc of the north Pamir. *Lithosphere* 2021. doi:10.2113/2021/6697858

Roberts, M. P., and Clemens, J. D. (1993). Origin of high-potassium, talc-alkaline, I-type granitoids. *Geol.* 21, 825–828. doi:10.1130/0091-7613(1993)021<0825:oohpta>2.3.co;2

Robinson, A. C., Ducea, M., and Lapen, T. J. (2012). Detrital zircon and isotopic constraints on the crustal architecture and tectonic evolution of the northeastern Pamir. *Tectonics* 31, 1–16. doi:10.1029/2011TC003013

Robinson, A. C. (2009). Geologic offsets across the northern Karakorum fault: Implications for its role and terrane correlations in the Western Himalayan-Tibetan orogen. *Earth Planet. Sci. Lett.* 279, 123–130. doi:10.1016/j.epsl.2008.12.039

Robinson, A. C. (2015). Mesozoic tectonics of the Gondwanan terranes of the Pamir plateau. *J. Asian Earth Sci.* 102, 170–179. doi:10.1016/j.jseaes.2014.09.012

Robinson, A. C., Yin, A., Manning, C. E., Harrison, T. M., Zhang, S.-H., and Wang, X.-F. (2007). Cenozoic evolution of the eastern Pamir: Implications for strain-accommodation mechanisms at the Western end of the Himalayan-Tibetan orogen. *Geol. Soc. Am. Bull.* 119, 882–896. doi:10.1130/B25981.1

Rutte, D., Ratschbacher, L., Khan, J., Stübner, K., Hacker, B. R., Stearns, M. A., et al. (2017a). Building the Pamir-Tibetan plateau—crustal stacking, extensional collapse, and lateral extrusion in the central Pamir: 2. Timing and rates. *Tectonics* 36, 385–419. doi:10.1002/2016TC004294

Rutte, D., Ratschbacher, L., Schneider, S., Stübner, K., Stearns, M. A., Gulzar, M. A., et al. (2017b). Building the Pamir-Tibetan plateau—crustal stacking, extensional collapse, and lateral extrusion in the central Pamir: 1. Geometry and kinematics. *Tectonics* 36, 342–384. doi:10.1002/2016TC004293

Ruzhentsev, S. V., and Shvol'man, V. A. (1981). Tectonic zoning of the pamirs and Afghanistan contemporary geoscientific researches in Himalaya: Dehradun Bishan Singh. Mahendra Pal Singh Publishers, 1, 53–59.

Safonova, I. Y., Utsunomiya, A., Kojima, S., Nakae, S., Tomurtogoo, O., Filippov, A., et al. (2009). Pacific superplume-related oceanic basalts hosted by accretionary complexes of Central Asia, Russian Far East and Japan. *Gondwana Res.* 16, 587–608. doi:10.1016/j.gr.2009.02.008

Saktura, W. M., Buckman, S., Nutman, A. P., and Bennett, V. C. (2021). Late jurassic changmar complex from the Shyok ophiolite, NW himalaya: A prelude to the ladakh arc. *Geol. Mag.* 158, 239–260. doi:10.1017/S0016756820000400

Schmidt, J., Hacker, B. R., Ratschbacher, L., Stübner, K., Stearns, M., Kylander-Clark, A., et al. (2011). Cenozoic deep crust in the Pamir. *Earth Planet. Sci. Lett.* 312, 411–421. doi:10.1016/j.epsl.2011.10.034

Schneider, F., Yuan, X., Schurr, B., Mechie, J., Sippl, C., Kufner, S. K., et al. (2019). The crust in the Pamir: Insights from receiver functions. *J. Geophys. Res. Solid Earth* 124, 9313–9331. doi:10.1029/2019JB017765

Schwab, M., Ratschbacher, L., Siebel, W., McWilliams, M., Minaev, V., Lutkov, V., et al. (2004). Assembly of the Pamirs: Age and origin of magmatic belts from the southern Tien Shan to the southern Pamirs and their relation to Tibet. *Tectonics* 23 (4). doi:10.1029/2003TC001583

Sengör, A. M. C. (1979). Mid-Mesozoic closure of permo-triassic tethys and its implications. *Nature* 279, 590–593. doi:10.1038/279590a0

Shvol'man, V. (1980). A Mesozoic ophiolite complex in the Pamirs. *Geotectonics* 14, 465–470.

Shvol'man, V. (1978). Relicts of the mesotethys in the pamirs. *Himal. Geol.* 8, 369–378.

Sobel, E. R., and Dumitru, T. A. (1997). Thrusting and exhumation around the margins of the Western Tarim basin during the India-Asia collision. *J. Geophys. Res.* 102, 5043–5063. doi:10.1029/96JB03267

Stearns, M., Hacker, B., Ratschbacher, L., Rutte, D., and Kylander-Clark, A. (2015). Titanite petrochronology of the Pamir gneiss domes: Implications for middle to deep crust exhumation and titanite closure to Pb and Zr diffusion. *Tectonics* 34, 784–802. doi:10.1002/2014TC003774

Stevens, G., Villaros, A., and Moyen, J.-F. (2007). Selective peritectic garnet entrainment as the origin of geochemical diversity in S-type granites. *Geol.* 35, 9–12. doi:10.1130/G22959A.1

Stübner, K., Ratschbacher, L., Rutte, D., Stanek, K., Minaev, V., Wiesinger, M., et al. (2013a). The giant Shakhdara migmatitic gneiss dome, Pamir, India-Asia collision zone: 1. Geometry and kinematics. *Tectonics* 32, 948–979. doi:10.1002/tect.20057

Stübner, K., Ratschbacher, L., Weise, C., Chow, J., Hofmann, J., Khan, J., et al. (2013b). The giant Shakhdara migmatitic gneiss dome, Pamir, India-Asia collision zone: 2. Timing of dome formation. *Tectonics* 32, 1404–1431. doi:10.1002/tect.20059

Sun, G., Hu, X., Sinclair, H. D., BouDagher-Fadel, M. K., and Wang, J. (2015). Late Cretaceous evolution of the Coqen Basin (Lhasa terrane) and implications for early topographic growth on the Tibetan Plateau. *Geol. Soc. Am. Bull.* 127, 1001–1020. doi:10.1130/B31137.1

Sun, S.-S., and McDonough, W. F. (1989). Chemical and isotopic systematics of oceanic basalts: Implications for mantle composition and processes. *Geol. Soc. Lond. Spec. Publ.* 42, 313–345. doi:10.1144/GSL.SP.1989.042.01.19

Sylvester, P. J. (1998). Post-collisional strongly peraluminous granites. *Lithos* 45, 29–44. doi:10.1016/S0024-4937(98)00024-3

Tadjidinov, K. S. (1988). "Paleovolcanic reconstructions and geological mapping (South Pamir)," in *Materials of the Central Asian regional petrographic meeting*. Editor L. Donish, 223–224.

Tang, Y., Zhai, Q., Hu, P., Xiao, X., and Wang, H. (2018). Petrology, geochemistry and geochronology of the zhongcang ophiolite, northern Tibet: Implications for evolution of the Bangong-Nujiang Ocean. *Geosci. Front.* 9, 1369–1381. doi:10.1016/j.gsf.2018.05.007

Tapponnier, P., Mattauer, M., Proust, F., and Cassaigneau, C. (1981). Mesozoic ophiolites, sutures, and arge-scale tectonic movements in Afghanistan. *Earth Planet. Sci. Lett.* 52, 355–371. doi:10.1016/0012-821x(81)90189-8

Valli, F., Leloup, P. H., Paquette, J. L., Arnaud, N., Li, H., Tapponnier, P., et al. (2008). New U-Th/Pb constraints on timing of shearing and long-term slip-rate on the Karakorum fault. *Tectonics* 27. doi:10.1029/2007TC002184

Villaros, A., Stevens, G., and Buick, I. S. (2009a). Tracking S-type granite from source to emplacement: Clues from garnet in the cape granite suite. *Lithos* 112, 217–235. doi:10.1016/j.lithos.2009.02.011

Villaros, A., Stevens, G., Moyen, J.-F., and Buick, I. S. (2009b). The trace element compositions of S-type granites: Evidence for disequilibrium melting and accessory phase entrainment in the source. *Contrib. Mineral.* . 158, 543–561. doi:10.1007/s00410-009-0396-3

Villarreal, D. P., Robinson, A. C., Carrapa, B., Worthington, J., Chapman, J. B., Oimahmadov, I., et al. (2020). Evidence for late triassic crustal suturing of the central and southern Pamir. *J. Asian Earth Sci. X* 3, 100024. doi:10.1016/j.jaesx.2019.100024

Volkmer, J. E., Kapp, P., Horton, B. K., Gehrels, G. E., Minervini, J. M., and Ding, L. (2014). Northern Lhasa thrust belt of central Tibet: Evidence of cretaceous–early cenozoic shortening within a passive roof thrust system. *Geol. Soc. Am. Special Pap.* 507, 59–70. doi:10.1130/2014.2507(03

Wang, B.-D., Wang, L.-Q., Chung, S.-L., Chen, J.-L., Yin, F.-G., Liu, H., et al. (2016). Evolution of the bangong–nujiang tethyan ocean: Insights from the geochronology and geochemistry of mafic rocks within ophiolites. *Lithos* 245, 18–33. doi:10.1016/j.lithos.2015.07.016

Wang, S., Tang, W., Liu, Y., Liu, X., and Yao, X. (2020a). Rushan-Pshart Paleo-Tethyan suture deduced from geochronological, geochemical, and Sr-Nd-Hf isotopic characteristics of granitoids in Pamir. *Lithos* 364, 105549. doi:10.1016/j.lithos.2020.105549

Wang, W., Wang, M., Zhai, Q.-G., Xie, C.-M., Hu, P.-Y., Li, C., et al. (2020b). Transition from oceanic subduction to continental collision recorded in the Bangong-Nujiang suture zone: Insights from Early Cretaceous magmatic rocks in the north-central Tibet. *Gondwana Res.* 78, 77–91. doi:10.1016/j.gr.2019.09.008

Wang, Y., Fan, W., Sun, M., Liang, X., Zhang, Y., and Peng, T. (2007). Geochronological, geochemical and geothermal constraints on petrogenesis of the indosinian peraluminous granites in the South China block: A case study in the hunan province. *Lithos* 96, 475–502. doi:10.1016/j.lithos.2006.11.010

Wang, Y., Zhang, Y., Fan, W., Geng, H., Zou, H., and Bi, X. (2014). Early Neoproterozoic accretionary assemblage in the Cathaysia Block: Geochronological, Lu–Hf isotopic and geochemical evidence from granitoid gneisses. *Precambrian Res.* 249, 144–161. doi:10.1016/j.precamres.2014.05.003

Whalen, J. B., Currie, K. L., and Chappell, B. W. (1987). A-Type granites: Geochemical characteristics, discrimination and petrogenesis. *Contrib. Mineral.* . 95, 407–419. doi:10.1007/BF00402202

Wood, D. A. (1980). The application of a Th-Hf-Ta diagram to problems of tectonomagmatic classification and to establishing the nature of crustal contamination of basaltic lavas of the British Tertiary Volcanic Province. *Earth Planet. Sci. Lett.* 50, 11–30. doi:10.1016/0012-821X(80)90116-8

Worthington, J. R., Ratschbacher, L., Stübner, K., Khan, J., Malz, N., Schneider, S., et al. (2020). The Alichur dome, South Pamir, Western India–Asia collisional zone: Detailing the Neogene Shakhdara–Alichur syn-collisional gneiss-dome complex and connection to lithospheric processes. *Tectonics* 39, e2019TC005735. doi:10.1029/2019tc005735

Xia, L.-Q. (2014). The geochemical criteria to distinguish continental basalts from arc related ones. *Earth-Science Rev.* 139, 195–212. doi:10.1016/j.earscirev.2014.09.006

Xia, L., and Li, X. (2019). Basalt geochemistry as a diagnostic indicator of tectonic setting. *Gondwana Res.* 65, 43–67. doi:10.1016/j.gr.2018.08.006

Xiao, W. J., Windley, B. F., Chen, H. L., Zhang, G. C., and Li, J. L. (2002). Carboniferous-Triassic subduction and accretion in the Western Kunlun, China: Implications for the collisional and accretionary tectonics of the northern Tibetan Plateau. *Geol.* 30, 295–298. doi:10.1130/0091-7613(2002)030<0295:ctsaai>2.0.co;2

Xu, Q., Zhao, J., Yuan, X., Liu, H., Ju, C., Schurr, B., et al. (2021). Deep crustal contact between the Pamir and Tarim Basin deduced from receiver functions. *Geophys. Res. Lett.* 48. doi:10.1029/2021GL093271

Xu, W., Liu, F., and Dong, Y. (2020). Cambrian to triassic geodynamic evolution of central Qiangtang, Tibet. *Earth-Science Rev.* 201, 103083. doi:10.1016/j.earscirev.2020.103083

Yang, W., Liu, L., Cao, Y., Wang, C., He, S., Li, R., et al. (2010). Geochronological evidence of Indosinian (high-pressure) metamorphic event and its tectonic significance in Taxkorgan area of the Western Kunlun Mountains, NW China. *Sci. China Earth Sci.* 53, 1445–1459. doi:10.1007/s11430-010-4081-1

Yin, A., and Harrison, T. M. (2000). Geologic evolution of the Himalayan-Tibetan orogen. *Annu. Rev. Earth Planet. Sci.* 28, 211–280. doi:10.1146/ANNUREV.EARTH.28.1.211

Yogibekov, D., Sang, M., Xiao, W., Windley, B. F., Mamadjonov, Y., Yang, H., et al. (2020). Late Palaeozoic to Late Triassic northward accretion and incorporation of seamounts along the northern South Pamir: Insights from the anatomy of the Pshart accretionary complex. *Geol. J.* 55, 7837–7857. doi:10.1002/gj.3906

Zanchetta, S., Worthington, J., Angiolini, L., Leven, E. J., Villa, I. M., and Zanchi, A. (2018). The Bashgumbaz complex (Tajikistan): Arc obduction in the cimmerian orogeny of the Pamir. *Gondwana Res.* 57, 170–190. doi:10.1016/j.gr.2018.01.009

Zanchi, A., and Gaetani, M. (2011). The geology of the Karakoram range, Pakistan: The new 1: 100, 000 geological map of central-western Karakoram. *Italian J. Geosciences* 130, 161–264. doi:10.3301/IJG.2011.09

Zanchi, A., Poli, S., Fumagalli, P., and Gaetani, M. (2000). Mantle exhumation along the tirich mir fault zone, NW Pakistan: Pre-mid-cretaceous accretion of the Karakoram terrane to the asian margin. *Geol. Soc. Lond. Spec. Publ.* 170, 237–252. doi:10.1144/GSL.SP.2000.170.01.13

Zanchi, A., Zanchetta, S., Berra, F., Mattei, M., Garzanti, E., Molyneux, S., et al. (2009). The eo-cimmerian (late? Triassic) orogeny in north Iran. *Geol. Soc. Lond. Spec. Publ.* 312, 31–55. doi:10.1144/SP312.3

Zhai, Q.-g., Jahn, B.-m., Su, L., Ernst, R. E., Wang, K.-l., Zhang, R.-y., et al. (2013a). SHRIMP zircon U–Pb geochronology, geochemistry and Sr–Nd–Hf isotopic compositions of a mafic dyke swarm in the Qiangtang terrane, northern Tibet and geodynamic implications. *Lithos* 174, 28–43. doi:10.1016/j.lithos.2012.10.018

Zhai, Q.-g., Jahn, B.-m., Su, L., Wang, J., Mo, X.-X., Lee, H.-y., et al. (2013b). Triassic arc magmatism in the Qiangtang area, northern Tibet: Zircon U–Pb ages, geochemical and Sr–Nd–Hf isotopic characteristics, and tectonic implications. *J. Asian Earth Sci.* 63, 162–178. doi:10.1016/j.jseaes.2012.08.025

Zhai, Q.-g., Jahn, B.-m., Wang, J., Hu, P.-y., Chung, S.-l., Lee, H.-y., et al. (2016). Oldest paleo-Tethyan ophiolitic mélange in the Tibetan Plateau. *Geol. Soc. Am. Bull.* 128, 355–373. doi:10.1130/B31296.1

Zhai, Q.-G., Jahn, B.-M., Zhang, R.-Y., Wang, J., and Su, L. (2011). Triassic subduction of the paleo-tethys in northern Tibet, China: Evidence from the geochemical and isotopic characteristics of eclogites and blueschists of the Qiangtang block. *J. Asian Earth Sci.* 42, 1356–1370. doi:10.1016/j.jseaes.2011.07.023

Zhang, K.-J., Zhang, Y.-X., Tang, X.-C., and Xia, B. (2012a). Late Mesozoic tectonic evolution and growth of the Tibetan plateau prior to the Indo-Asian collision. *Earth-Science Rev.* doi:10.1016/j.earscirev.2012.06.001

Zhang, Q., Ran, H., and Li, C. (2012b). A-type granite: What is the essence? *Acta Petrologica Mineralogica* 31, 621–626. (in Chinese with English abstract).

Zhang, Z., Zhao, G., Santosh, M., Wang, J., Dong, X., and Shen, K. (2010). Late cretaceous charnockite with adakitic affinities from the gangdese batholith, southeastern Tibet: Evidence for neo-tethyan mid-ocean ridge subduction? *Gondwana Res.* 17, 615–631. doi:10.1016/j.gr.2009.10.007

Zhao, Z., Bons, P. D., Wang, G., Soesoo, A., and Liu, Y. (2015). Tectonic evolution and high-pressure rock exhumation in the Qiangtang terrane, central Tibet. *Solid* 6, 457–473. doi:10.5194/se-6-457-2015

Zheng, H., Huang, Q. T., Cai, Z. R., Zhang, K. J., Liu, H. C., Cheng, C., et al. (2019). Early Cretaceous arc granitoids from the central Lhasa subterrane: Production of the northward subduction of yarlung zangbo neo-tethyan ocean? *Geol. J.* 54, 4001–4013. doi:10.1002/gj.3399

Zheng, Y.-F., and Gao, P. (2021). The production of granitic magmas through crustal anatexis at convergent plate boundaries. *Lithos* 402403, 106232. doi:10.1016/j.lithos.2021.106232

Zhu, D.-C., Li, S.-M., Cawood, P. A., Wang, Q., Zhao, Z.-D., Liu, S.-A., et al. (2016). Assembly of the Lhasa and Qiangtang terranes in central Tibet by divergent double subduction. *Lithos* 245, 7–17. doi:10.1016/j.lithos.2015.06.023

Zhu, D.-C., Zhao, Z.-D., Niu, Y., Dilek, Y., Hou, Z.-Q., and Mo, X.-X. (2013). The origin and pre-Cenozoic evolution of the Tibetan Plateau. *Gondwana Res.* 23, 1429–1454. doi:10.1016/j.gr.2012.02.002

Zhu, R.-Z., Lai, S.-C., Qin, J.-F., Zhao, S.-W., and Santosh, M. (2018). Strongly peraluminous fractionated S-type granites in the Baoshan Block, SW China: Implications for two-stage melting of fertile continental materials following the closure of Bangong-Nujiang Tethys. *Lithos* 316, 178–198. doi:10.1016/j.lithos.2018.07.016

Zhu, Y., Lai, S.-c., Qin, J.-f., Zhu, R.-z., Zhang, F.-y., and Zhang, Z.-z. (2020). Petrogenesis and geochemical diversity of late mesoproterozoic S-type granites in the Western yangtze block, south China: Co-Entrainment of peritectic selective phases and accessory minerals. *Lithos* 352, 105326. doi:10.1016/j.lithos.2019.105326